UNIVERSITY OF THESSALY

POLYTECHNIC SCHOOL

DEPARTMENT OF MECHANICAL ENGINEERING

LABORATORY OF MATERIALS

Diploma Thesis

Study of the microstructure and the mechanical properties of the aerospace aluminum alloy 7075 using the computational software TC-PRISMA

By

Antonaki Fotini

Supervisor:

Dr. Helen Kamoutsi

Submitted for the Partial Fulfillment of the requirements for

the degree of Diploma in Mechanical Engineering

Certified by the members of the Thesis Committee:

First Examiner Dr. Helen Kamoutsi

(Supervisor) Lab Teaching Staff

Department of Mechanical Engineering

University of Thessaly

Second Examiner Dr. Gregory. N. Haidemenopoulos

Professor of Physical Metallurgy

Department of Mechanical Engineering

University of Thessaly

Third Examiner Dr. Alexis Kermanidis

Professor of Mechanical Behavior of Materials

Department of Mechanical Engineering

University of Thessaly

Table of Contents

Table of Figures

Table of Tables

Acknowledgements

This project was accomplished in the scope of the partial fulfillment of the requirements for the degree of Diploma in Mechanical Engineering at University of Thessaly.

I would first like to express my sincere appreciation to my supervisor Dr. Helen Kamoutsi, without her persistent help, the goal of this project would not have been realized.

Further, I am particularly grateful to Professor Gregory N Haidemenopoulos and Professor Alexis Kermanidis for accepting to take part in the three-member evaluation committee of my Diploma Thesis.

I would also like to express my gratitude to my whole family, especially to my parents, Christiana and Vaggelis, for their continuous support during my studies.

Abstract

The aluminum alloy AA7075 is a lightweight heat treatable alloy with multiple applications in aerospace and military aerospace structures. It belongs to the 7xxx series, or in other words to Al-Zn-Mg(-Cu) alloys. The unpropitious conditions that 7xxx alloys are summoned to deal, require very strict limits in properties like the resistance to stress corrosion cracking. Hardening by aging is the most usual and efficient hardening treatment for these alloy series. The main hardening phase in this type of alloys, is the metastable η' phase, which is a precursor to the equilibrium η ($MgZn_2$) phase. Even the many studies that have been made on the microstructure phenomena during aging precipitation, for the Al-Zn-Mg(-Cu) alloys, some points remain controversial. The last decades, modeling of the aging precipitation using various calculating software, has also been a subject of investigation. Driven by the strict requirements and scientific interest for the Al-Zn-Mg(-Cu) alloys, this thesis intends to study the microstructure phenomena during aging precipitation and correlate them to the evolution of hardness during aging. In the context of this study, a bibliographic review, followed by experimental procedures like optical metallography and microhardness measurements, and finally, by simulating an aging treatment with the TC-PRISMA precipitation module, were proceeded.

Chapter 1 Introduction

The aluminum alloy AA7075, as all the alloys of 7xxx series, is a lightweight heat treatable alloy with multiple applications in aerospace structures. Its excellent properties, like its resistance to stress corrosion cracking, occur due to suitable heat treatments. The aluminum alloys of 7xxx series usually consist of zinc and magnesium, while sometimes they contain small additions of copper (no more than 3%). The main strengthening treatment for these alloys, is the aging heat treatment. The preparatory procedures applied in these alloys need great attention in order for their properties to comply with the strict limits that the challenging conditions of their many applications (aerospace and military aerospace structures) require.

Aging strengthens the material by the precipitation mechanism, during which a fine dispersion of precipitates forms and impede the dislocations slide. Previously to aging heat treatment, a solution treatment with a subsequent quench of the material is required. Solution treatment aims at increasing the solubility limits of the alloy contents and thus, creating a homogeneous solid solution, by isothermal heating close to eutectic temperatures. By quenching the material at low temperatures, a supersaturated solid solution occurs, and a driving force for precipitation develops. Aging treatments can be natural (aging at room temperature), during which the precipitation results only by the supersaturation, or artificial (intermediate temperatures), during which the precipitation is also assisted by the higher diffusion rates. A usually applied artificial treatment, with better results of hardening, is the duplex aging. This treatment consists of two aging treatments. The first takes place at low temperatures, where the driving force for precipitation occurs only due to the high supersaturation. At this step the precipitates nucleate rapidly. Then, at relatively higher temperatures in the second treatment, the nucleated particles are allowed to grow faster due to the higher diffusion rates.

The precipitation starts with the nucleation of particles at preferential sites, like each atom in the matrix for homogeneous nucleation, or structure defects for heterogeneous. The first particles that the system prefers to nucleate, are coherent metastable phases instead of the incoherent equilibrium phases due to their lower interfacial energy. Subsequently though, the system prefers to lose gradually the coherency between the precipitates and the matrix, because of the high strain energy of a coherent interface. The coherency loss is achieved by the transformation of coherent to semicoherent phases and finally to incoherent phases. This phenomenon results in characteristic transition sequences for each type of alloy. After the nucleation process ends, the growth of the precipitates starts. During this process the precipitates grow due to diffusion of solute atoms from the matrix towards them. Growth ends when the new phase composition reaches the equilibrium according to the relative phase diagram. Even at this state, the system seems to have reached an equilibrium state, its interfacial energy is still high and thus. Hence, in practice is still metastable and starts to reduce its free energy by the coarsening process. During this process the density of precipitates decreases, and the size of the precipitates grow, resulting to a coarsen distribution of precipitates incapable of obstructing the dislocations slide. Therefore, coarsening is an unwanted effect for the precipitation strengthening.

Even the numerous studies on the microstructure characteristics of precipitation (such as precipitate phases and the kinetics of their transformations) in aluminum alloys of 7xxx series, some points remain controversial for the scientific community. However, the most established transition sequence for the aluminum 7xxx type of alloys is:

$$SSSS \rightarrow GP\ zones \rightarrow \eta'\ (metastable\ phase) \rightarrow \eta\ (equilibrium\ MgZn_2\ phase)$$

GP zones, in other terms Guinier Preston zones, are zones of precipitates presented in many types of aluminum alloys as the first coherent precipitate phase. The metastable η' phase is a precursor of the equilibrium η phase and is considered the main hardening phase for this series of alloys. Some studies though include also the GP zones to the main hardening phases of 7xxx series alloys.

During the last decades, predicting the microstructure behavior during aging precipitation has been a subject of many studies. The reason behind of these investigations is that a simulation of precipitation process with good accuracy, could be a helpful tool for digital alloy and process design. A numerical model, proved to give accurate results, is the KWN (Kampmann-Wagner) model. According to this model, which is an extension of the Langer-Schwartz (LS) theory, the particle size distribution (PSD) is an expression of the precipitation evolution. To solve the complex problem that occurs, KWN method discretizes the PSD and solves it directly.

Based in the scientific and industrial interest that the 7xxx alloys present, the objective of this study is to gain more information about the aging precipitation phenomena in the microstructure and how they are correlated with the hardness evolution during aging, as well as the response of the AA7075 alloy in various aging treatments. To achieve this, the AA7075 studied alloy was subjected to optical metallography, and microhardness measurements after various aging treatments. Finally, a simulation of an aging treatment was attempted using the TC-PRISMA precipitation module.

Thesis Outline:

Chapter 1 - Introduction

Chapter 2 - Bibliographic Review

Chapter 3 - Methodology

Chapter 4 - Results

Chapter 5 - Conclusions

Chapter 2 Bibliographic Review

2.1 Properties and characteristics of AA7075 and 7xxx alloy series

The aluminum alloy 7075 belongs to the high strength 7xxx series and find multiple applications at aerospace structures like fuselage frames and wing skins. The 7xxx aluminum alloys are known for their machinability and weldability as well as their high resistance to stress corrosion cracking after suitable treatments [1]. As heat treatable alloys, their strengthening is usually achieved by aging treatments. Their ternary system consists of aluminium, zinc and magnesium, while in some cases, small amounts of copper may be also contained. Zinc is found in a range of 1 to 8% in these alloys, and its addition increase the solution potential of the alloy. Magnesium, specifically in amounts of 3 to 7.5%, appears to increase the strengthening potential of the alloy [2]. The copper containing alloys, like the AA7075, are assumed to share the same precipitation sequence and similar precipitation mechanisms with the Al-Zn-Mg alloys [3]. However, the Al-Zn-Mg-Cu alloys seem to have better response to hardening heat treatments. Specifically these alloys that also contain small but important amounts of chromium and manganese are considered the highest-strength aluminum alloys available [2].

2.2 Strengthening by Aging

Aging treatment is one of the most important strengthening methods and it is applied to a wide range of alloys, including aluminum alloys. In this process, the alloy is strengthened by the mechanism of precipitation, a diffusional phase transformation. During aging, a fine dispersion of precipitates is created, capable of obstructing the dislocation slide and increasing the material strength.[4]

Before the aging process, two other treatments are required. The first treatment is isothermal heating above the solvus temperature. This process aims to maximize the solid solubility of the additional alloying elements to create a homogeneous solid solution of an aluminum matrix with excess vacancies. Immediately after this solution treatment, the material is subjected to rapid cooling (quenching) at room temperature. Due to the lack of time, the precipitation of equilibrium phases is prevented, and the excess vacancies are retained in the matrix. As a result, a supersaturated solid solution (SSSS) is produced, causing a significant driving force for precipitation. In the final aging heat treatment, nucleation and growth mechanisms are activated, creating a fine distribution of hardening precipitates. [4]

2.2.1 Solution Heat Treatment

As stated above, the purpose of the solution heat treatment is to attain a homogeneous microstructure of a single phase by dissolving all the other contained phases. This treatment takes place at temperatures above the solvus where the solubility of additional elements reaches a maximum [4]. However, some phases, such as constituent particles that containing impurity elements, cannot dissolve during solution treatment [5]. Choosing the suitable solution temperature is of high importance, because of the defects that may occur due to overheating or underheating of the material. Heating the material above the eutectic melting points, may lead to degradation of other properties like tensile strength or ductility. On the other hand, solution treatments at significantly lower temperatures than the solvus do not allow the material to attain the maximum expected strength. The suitable temperature for complex systems, such as ternaries or quaternary, depends on how the additional alloying elements affect the solid solubility and the eutectic melting points of the basic binary system. Another important factor that helps to achieve the highest homogeneity that is possible is time. The required time is determined by the initial microstructure of the material and the size of the piece [6].

2.2.2 Quenching

In quenching, the material is cooled rapidly at room temperature by soaking it in cold water. The rapid cooling after the solution treatment aims to retain the homogeneous microstructure with the excess vacancies at room temperatures, preventing any precipitation which would occur by slow cooling. Hence, the solid solution becomes supersaturated in solute atoms and vacancies, and a big driving force for precipitation is created. [4,6] Direct and fast cooling after the solution treatment is of high importance, because if sufficient precipitation occurs prior to that the hardness will never reach the expected maximum value[6]. The precipitated particles in slow cooling such as dispersoids cannot contribute to obstructing the dislocations movement, because of their size and their distribution, while their formation depletes the matrix of solute and consequently reducing the amount of the subsequent hardening precipitates[3]. Therefore, the quench sensitivity of an alloy, i.e., how much the quenching rate affects its final hardness, depends on the included heterogeneities (dispersoids, grain boundaries) which act like heterogeneous nucleation sites reducing the precipitation abilities. [7]

2.2.3 Aging Heat Treatment

Aging is the final stage of the hardening process where the optimal hardness is achieved. Aging is distinguished in two types with respect to the temperature that precipitation takes place, natural and artificial [4]. In natural aging, the pr63ecipitation occurs spontaneously at room temperature only by the supersaturation of solute atoms and vacancies, while in artificial aging, the process of precipitation is also assisted by the higher diffusional rates at intermediate temperatures leading to faster results. Some aluminum alloys, such as the 7xxx series, are considered unstable in natural aging conditions because their mechanical properties continue to change over a long period of time. Hence, artificial aging is required in these cases [6].

Reaching the maximum hardness value usually comes along with degradation of other mechanical properties. Thus, the industrial purpose of age hardening is not to reach the peak hardness, but to reach the possible maximum value without sacrificing the lower limits of other properties, depending each time on the needs of the application [5]. To achieve this, a variety of multistage treatments has been developed for industrial practice. As an example, the as called duplex aging, or two-step aging, not only gives better results in hardness, but also increases the stress-corrosion resistance in the aluminum alloys of 7xxx series [8]. The first step of this treatment is a natural or an artificial at low temperatures aging for a short period of time. During this step, homogeneous nucleation occurs because of the high supersaturation. In the second step, which is an artificial aging at higher temperatures, the precipitates grow faster because of the higher diffusional rates. As a result, a finer distribution of precipitates is achieved with respect to the one-step aging's [5,9]. Other aging methods may contain treatments like cold work or heating at temperatures where retrogression of precipitates occurs [8].

2.2.4 Aging Temper Designations

According to the temper designation system for aluminium and aluminum products, the main tempers for aging treatments are:

- W expresses the unstable condition of Al-Zn-Mg alloys after natural aging.
- T6 temper stands for solution heat treated and artificial aged until peak hardness materials.
- T7 represents overaged materials, providing this way higher resistance in stress corrosion cracking than the T6 temper.

2.3 Kinetics of Precipitation Transformation

Precipitation is a diffusional thermal activated transformation, during which the stable and the metastable phases form by the mechanisms of nucleation and growth. The nucleation of a new phase starts when a strong local variation in composition is created. After their formation, nuclei grow into precipitates by diffusion of solute from the matrix towards them. [4,10]

2.3.1 Nucleation of Precipitates

As stated previously, the chemical driving force for precipitates nucleation depends on the rate of supersaturation caused by the quench. A numerical expression of this driving force is:

$$\Delta G_V = -\frac{RT}{V_m}\, ln\frac{c_0}{c} \qquad 2.1$$

Where V_m is the molar volume of the precipitate phase, R is the universal gas constant, c_0/c is the supersaturation ratio, c_0 and c is the chemical composition of the alloy and the composition of the matrix in the supersaturated solid solution (SSSS) respectively.

The total variation of system free energy because of precipitates nucleation is due to three factors. Firstly, the volume creation of a stable phase leads to a reduction of the free energy. However, the interfacial energy is increased because of the new nuclei interface. Furthermore, the formation of the precipitates inputs strain in the system resulting also to an increase of its free energy. Therefore, this variation can be written as a function of these three factors:

$$\Delta G = V\Delta G_V + \gamma_{\alpha\beta}A + V\Delta G_\varepsilon \qquad 2.2$$

Where V is the volume of the nuclei, $\gamma_{\alpha\beta}$ is the interfacial energy of the A new surface and ΔG_ε is the strain energy

A nucleation process that is not assisted by any structural defects such as dislocations, grain boundaries or vacancies, is characterised as homogeneous. Thermodynamical analysis with the assumption of spherical precipitates shows that activation energy for homogeneous is very high. On the contrary, in heterogeneous nucleation, the assistance of structural defects seems to reduce the activation energy for nucleation making them preferable sites for nuclei formation. Hence, in most cases the nucleation is heterogeneous.

2.3.1.1 Coherency loss

During precipitation, a continuous competition takes place between the contributions of interfacial and strain energy, to the activation energy. At the beginning of nucleation, when the particles size is still small, they are in complete coherence with matrix. Even coherency strain energy is high, the system prefers this state because of the much higher interfacial energy that an incoherent boundary would provoke. After a critical particle size, the value of the interfacial energy becomes higher than the value it would obtain under semicoherency circumstances. Therefore, the system chooses to lose its total coherency. This transition is described for spherical precipitates, by the graph in Figure 2.1. In the region before the critical radius the free energy ΔG of coherent interfaces is lower than this semicoherent, while in the region after the critical radius the reverse applies. As the particle grow, for the same reason, the system will choose to form incoherent interfaces. This process that begins from the nucleation and continues during the growth of the precipitates is called coherency loss.[1] However, in practice, there is a required condition that makes difficult for a particle to lose its coherency with the matrix. This condition is the presence of dislocation loops around the particle.[10]

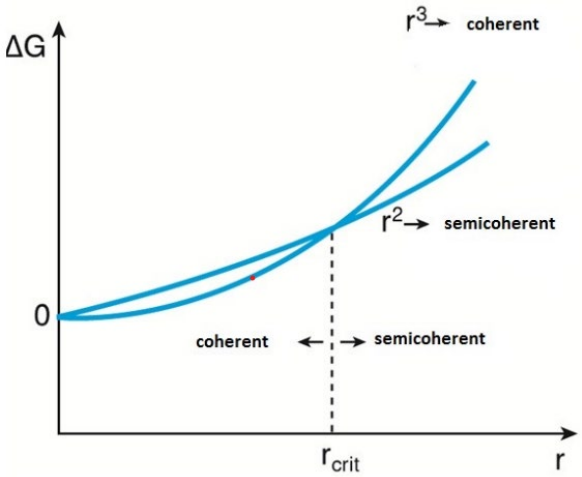

Figure 2.1: The free energy of the system ΔG for coherent and semicoherent interfaces, in relation to the radius of the precipitates

There are several mechanisms by which this condition is satisfied, and the coherency loss occurs. The simplest mechanism may take place in spherical precipitates when the values of the stresses at their interfaces get higher than the theoretical matrix strength (estimated critical value of stresses ε_{crit} = 0.05). Then, there are possibilities that a dislocation loop passes through the interface of the precipitate, like the illustration in Figure 2.2(a). Note that this process is independent of particle size. Consequently, no matter if a precipitate is bigger than the critical size, this mechanism may never occur. On the contrary, another mechanism for spherical shapes, during which dislocations depending on their Burgers vectors may be attracted by the particle interface and be forced to wrap around it, requires greater particle size than the critical. This process, simulated in Figure 2.2(b), can be assisted by mechanical deformation during aging but is rare in annealed materials. [10]

When it comes to plates, the coherency loss occurs with different ways. The great stresses that grow at the plate edges can exceed the matrix' theoretical strength. Hence, in this case the precipitate itself produce dislocations. A significant property of this process is that it can happen repeatedly as the plate length grows, like it appears in Figure 2.2(c). There is also a mechanism, in which vacancies are collected at coherent interfaces and form a prismatic dislocation loop which can surpass the precipitate as it is simulated in Figure 2.2(d).[10]

Coherency loss is an explanation for the fact that instead the incoherent equilibrium formation the alloying system prefers to initially precipitate incoherent and semicoherent phases, called transition or metastable phases. This way, a transition sequence is created for each alloying system precipitation.

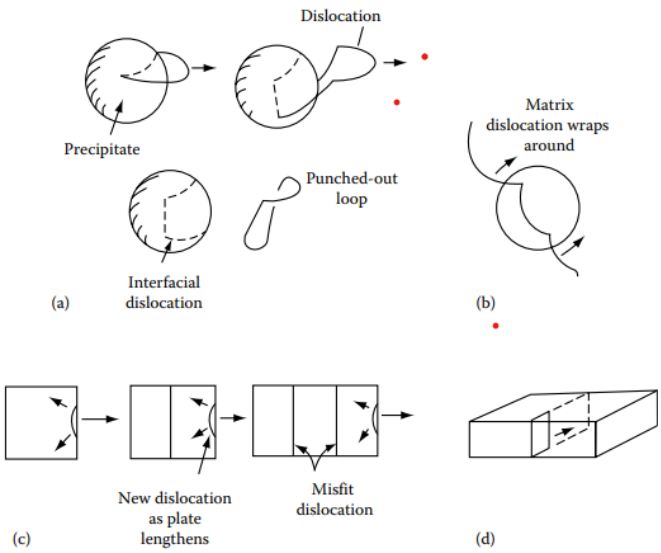

Figure 2.2: "Mechanisms for coherency loss, (a) Dislocation punching from interface, (b) Capture of matrix dislocation, (c) Nucleation at edge of plate repeated as plate lengthens, (d) Loop expansion by vacancy condensation in the precipitate." [10]

2.3.1.2 Nucleation sites

There are several types of nucleation sites, except of homogeneous sites which contain every atom in the aluminum matrix, structural defects like grain boundaries, vacancies and dislocations can also be nucleation sites. The type of nucleation sites that a system prefers during precipitation depends on the driving force for precipitation as well as each type's concentration and potential to decrease the activation energy. The different types of nucleation sites are presented in Table 2.1 from the type with the highest potential to reduce the activation energy for nucleation (at the top of the table) to the type with the lowest one (at the bottom of the table). According to this sequence the system should always prefer free surfaces or grain and antiphase boundaries as nucleation sites. The value of driving force though is capable to affect this preference. In cases of lower driving forces, the dominant nucleation sites are indeed grain corners and boundaries. However, when the driving force is extremely high, the homogeneous sites lead to higher nucleation rates and hence, they are preferred for nucleation.

Nucleation sites arranged in order of decreasing the activation energy for nucleation
free surfaces
grain and interphase boundaries
stacking faults
dislocations
vacancies
homogeneous sites

Table 2-1: Nucleation sites arranged in order of decreasing the activation energy for nucleation (highest to lowest) [10]

2.3.2 Growth of Precipitates

Growth is a process that starts after the nucleation and is completed when the new phase reaches the equilibrium concentration according to the relative phase diagram. A precipitate grows due to the movement of its interphase boundaries into the matrix. The precipitation growth belongs to civilian

transformations, during which the interfaces move by unsynchronized diffusion of atoms across non-glissile interfaces. [4,10]

Depending on the equilibrium concentration of the new phase the growth can be distinguished in two categories. If the concentration of the new phase is the same as in the matrix, the growth is considered as interface controlled, while in cases that these concentrations are different the growth may be under both interfacial and diffusional control. These two types of growth may coexist and when both of their rates are significant the growth process occurs under mixed control. In interface-controlled growth the diffusion rate is high, and the growth rate depends on how fast the atoms can pass through an interface. On the contrary, in diffusional control, the atoms can easily cross the interface, but the growth rate depends on how fast the diffusion happens. [4,10]

Figure 2.3 shows a simple example of growth in precipitation. As it appears in Figure 2.3(a), the alloy with concentration equal to c_0 is cooled rapidly from temperature T_1, where the α phase is a homogeneous solid solution, to temperature T_0, where the solid solution is supersaturated with a driving force to precipitate β phase. The free energy diagram (Figure 2.3(b)) shows that the system can go to a state with lower free energy by forming the β phase. The chemical driving force for this process is represented in the diagram by the TL section. Figure 2.3(c) presents the concentration profile in B component during growth. The interface movement here, and thus the precipitate growth, occurs by the diffusion of solute atoms (B atoms for the example) from the matrix (α) into the new phase (b). In the interior of the β phase the concentration remains steady at the equilibrium value of c_β and reduces rapidly at its interface (c_i). The concentration of the α phase, though, appears a variation, starting from the solid solution concentration c_0 at a long distance from the interface and gradually reducing to the interface value c_i. In cases that local thermodynamical equilibrium occurs at the interface, i.e., interface concentration is equal to the equilibrium concentration c_α, the growth is under diffusional control. On the contrary, an interface concentration, equal to this of the initial solution, indicates that growth is interface controlled. For intermediate concentration values, the control of the process is considered as mixed.[4]

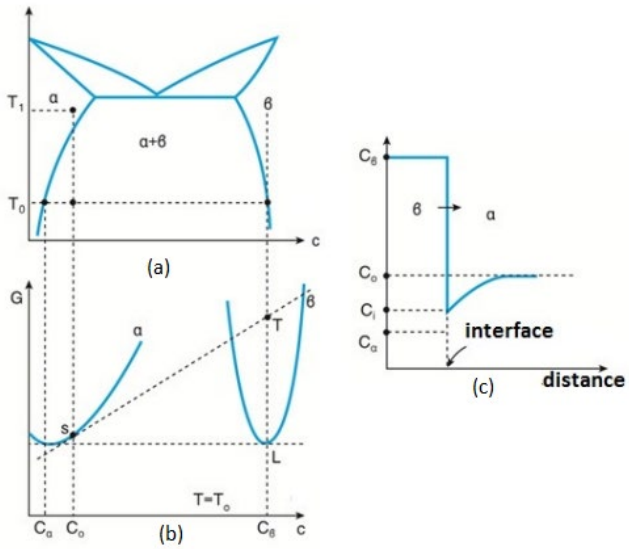

Figure 2.3: (a) phase diagram A-B, (b) free energy diagram at T_0 temperature, (c) concentration profile during growth

2.3.3 Excess Vacancies

During solution treatment the alloy contains a high concentration of vacancies because of the elevated temperature. By a low cooling rate these vacancies would gradually reduce to the equilibrium concentration of lower temperatures, because of the quench though, the system does not have the required time to do it. As a result, the quenched in vacancies are found in excess of the equilibrium concentration in the supersaturated solution. To reach the equilibrium state, the vacancies anneal out or cluster with solute atoms creating vacancy rich clusters (VRC) [11].

The excess vacancies may play various roles in precipitates nucleation and growth according to bibliography. Firstly, the presence of vacancies makes it easier for solute atoms to diffuse into the aluminum matrix, increasing this way the diffusional rate and thus the nucleation and growth rates. This effect is an explanation to the rapid nucleation that can occur even at room temperature (natural aging) for some alloys. In addition, vacancies and VRCs can be considered as dominant nucleation sites during the precipitation since their concentration exceeds the equilibrium's. The quenched in vacancies also appear to play an essential role to the precipitate free zones (PFZ) formation, a defect that can occur during precipitation strengthening and will be discussed later [10].

2.3.4 Precipitate Free Zones (PFZ)

In many cases after aging, zones denuded by precipitates in the vicinity of grain boundaries appear. These zones are called precipitate free zones (PFZ) and are a common defect in precipitation processes. There are two possible explanations for this phenomenon, and both are associated with the grain boundaries. According to the first, the grain boundaries which function as sinks of vacancies, deplete their adjacent matrix regions from vacancies. Considering that vacancies are one of the main sites for nucleation, no precipitation will take place in these regions, even if the matrix concentration in solute remains the same with the interior of the grain [5,10–14]. Except of vacancies sinks though, the grain boundaries are preferable sites for heterogeneous nucleation. Hence, the other theory of the PFZ formation is based on the solute depletion of these zones because of precipitation in grain boundaries [5,10,13,14]. Between these two mechanisms, the most usual to occur is the former, because of there are no intense fluctuations in the matrix's concentration [12–14]. The latter mechanism appears only in regions very close to boundaries [14]. For the same reasons, PFZ can also appear in the vicinity of inclusions or dislocations [10].

Several steps can be taken during the treatments of precipitation strengthening in purpose of eliminating the PFZ. Fast quenching rates can prevent the vacancies depletion in the vicinity of structure defects resulting in narrower PFZs. Narrower PFZs also occurs at low aging temperatures. The high driving force for precipitation, because of the high supersaturation at these temperatures, leads to almost homogeneous nucleation, during which vacancies are not the dominant nucleation sites. Duplex aging seems to give even better results, assuring homogeneous nucleation in the first aging step at low temperatures, and faster growth rates at the relatively higher temperatures of the second step [10].

2.3.5 Overall Precipitation Kinetics

Tthe mechanisms for precipitation transformation are nucleation and growth, of which the kinetics were discussed previously. Hence, the total velocity of the transformation depends on both nucleation and growth rates. The two factors that proved to affect these rates, is the chemical driving force for precipitation as well as the diffusion rate which both depend on the temperature of the transformation [4].

The diagram in Figure 2.4 is a qualitative expression of the transformation temperature dependence. The curve is called C-curve kinetics because of its shape and represents the total kinetics of the transformation with respect to aging temperature. At low aging temperatures, even if the supersaturation ratio and thus the driving force are high, the mechanism is carried out with a slow rate because of the low diffusional rates. Similarly, at high temperatures, close to the solvus temperature, the transformation is the same slow due to the low driving force (even at these temperatures diffusion is fast). The best results for the precipitation rate are given at intermediate temperatures according to the diagram, where both supersaturation and diffusion can contribute efficiently [4].

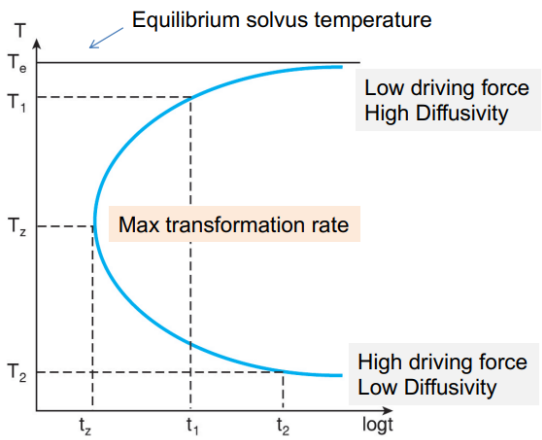

Figure 2.4: Temperature dependence of the precipitation transformation [4]

By expanding the study of the previous example of a simple precipitation reaction, a better understanding of the transformation's evolution can be achieved. The numerical expression for precipitation progress, is the f transformation fraction, plotted with respect to temperature and time. The f fraction in precipitation reactions, is represented by the volume fraction of the precipitated β phase divided by the equilibrium volume fraction of β phase. The values of the fraction fluctuate from zero at the start of the transformation, to one when the equilibrium state is reached. The information about the function f (t, T) can be given from Isothermal Transformation (IT) diagrams. Figures 2.4(a and b) show the association between an IT diagram is associated and the f(t) transformation fraction. Fig.2.4(a) presents the two C curves, standing for the start and the end of the transformation respectively. In Fig.2.4(b), the evaluation of the f fraction over time is illustrated for temperatures T_Z and T_1. At T_Z intermediate temperature, the precipitation transformation happens faster than at the high temperature T_1 [4,10].

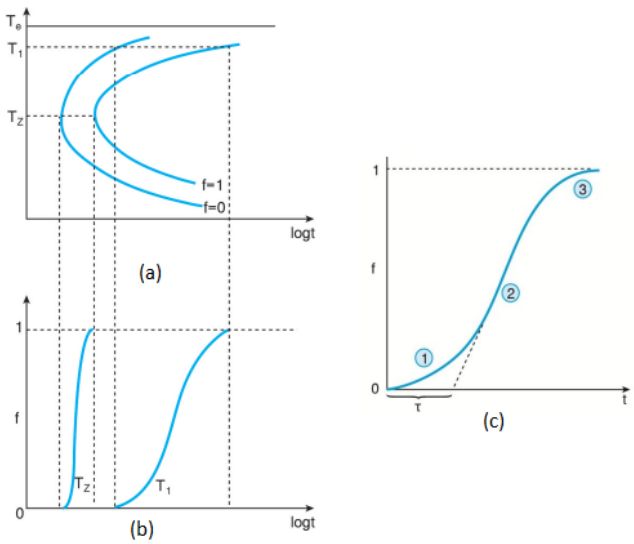

Figure 2.5: (a) IT diagram, (b) respective diagram of transformation fraction f as a function of time for different temperatures, (c) f(t) curve divided in three periods, 1: induction, 2: growth, 3: impingement

The S shaped curve is characteristic of the f(t) function, and it can be divided into three periods. The first period, symbolized with the letter τ in Fig.2.4(c), is called induction and represents the time that nucleation process takes to complete. The second period is the growth of the precipitates, which ends a little before the transformation is completed. At this point, the precipitates have grown at such a size that there is possibility for particles to meet creating an interface β/β and their growth stops. Thus, during the impingement period the growth rates reduce again. [4]

For the mathematical analysis of the transformation kinetics, the assumption of random nucleation sites distribution should be taken. A volume V, which is initially occupied by α phase, and finally by β phase is considered as system reference for this analysis. An equation that describes well the kinetics of the initial stages of the transformation is:

$$f = \frac{\pi}{3} I u^3 t^4 \qquad 2.3$$

Where I is the nucleation rate, u is the growth velocity, and t is the time. This equation though, is unsuitable for the stages of significant impingement of precipitated particles. Johnson and Mell as well as Avrami, to express mathematically the reduction in the growth rate, caused by the impingement effect, made the following assumption: During the induction period, some imaginary nuclei form into the already formed β phase. These nuclei are the hypothetical nuclei that could form, if a precipitate could grow into another, in other words if no impingement effect occured. As a result, a new volume of phase β would form, different form the real one. The analysis of the mathematical relationship between this volume (named extended volume in bibliography) and the real one leads to the following expression, called and Johnson-Mehl equation:

$$-\ln(1-f) = \frac{4}{3}\pi u^3 \int_0^t I(t-\tau)^3 \, d\tau \qquad 2.4$$

The above equation can be solved only by making assumptions about the nucleation rates. A general expression of the precipitation kinetics which takes account the impingement phenomenon is the Johnson-Mehl-Avrami-Kolmogorov (JMAK) equation:

$$\mathrm{f} = 1 - \mathrm{e}^{-\mathrm{kt}^{\mathrm{n}}} \qquad 2.5$$

where k is a constant, which depends on nucleation and growth rates and thus, the temperature, and n is a constant with values in the range of 3 to 4. The equation 2.5 gives satisfying results for linear growth, i.e., the precipitates' radius is a linear function of time, but also for initial stages of diffusional controlled growth, where the radius is proportional to $t^{1/2}$. [4]

2.3.6 Coarsening of precipitates

In the end of the precipitation transformation, i.e., the end of the growth, the fractions of the phases have reached the equilibrium values, predicted from the respective phase diagram. Hence, it is assumed that the system has reached a thermodynamical equilibrium state. However, the interfacial energy of the system is not minimum, because of the interphase boundaries. Consequently, in practice, the system is still in a metastable state. In order to eliminate its interfacial energy, the system tends to reduce the density of the precipitates and increase their size. The transition from the fine dispersion, achieved by the precipitation process, to a dispersion with less but bigger precipitates is called coarsening. As the precipitates coarsen, the dislocations are allowed to move freely again in the alloy's matrix, and the hardness reduces. Moreover, the coarsening rates increase with increasing temperature, and hence, the coarsening defect is a high importance subject in high temperature applications. [4,10]

A thermodynamical and kinetic analysis of coarsening mechanism assists to better understand and control the phenomenon. In the end of the growth, a wide range of precipitates' size exists because of the heterogeneous nucleation and the different growth rates. Because of the free energy dependence on the radius of the curvature, called and Gibbs-Thomson effect, solute atoms diffuse from smaller to bigger particles through the matrix. As a result, the precipitates of smaller sizes shrink until they disappear, while the of larger size continue to grow. [4]

The Gibbs-Thomson effect is well explained in Fig.2.6(a). Corresponding to the previous example of precipitation, two different size particles of the precipitated phase β (r_1>r_2) are presented in Fig.2.6(b). The free energy diagram shows that the smaller the size of the particle is, the higher its free energy. The expression of this effect, i.e., the correlation between the free energy (ΔG), and the radius of curvature (r), is given in the following equation 2.6. The term γ represents the interfacial energy, while V_m the molar volume of the β phase. The assumed final state of coarsening is the ideal state where the precipitate's radius of curvature tends to infinity.

$$\Delta G = \frac{2\gamma V_m}{r} \qquad 2.6$$

In the diagram of Fig.2.6(a), the free energy of β phase's precipitate is represented by the segment between equilibrium states of radius r and infinite radius. This segment can be assumed to also represent a chemical driving force for diffusion, from the interfaces with small curvature radius, to interfaces with large curvature radius. During coarsening process, the fraction of β phase remains steady but the mean radius of the dispersion increases over time [4].

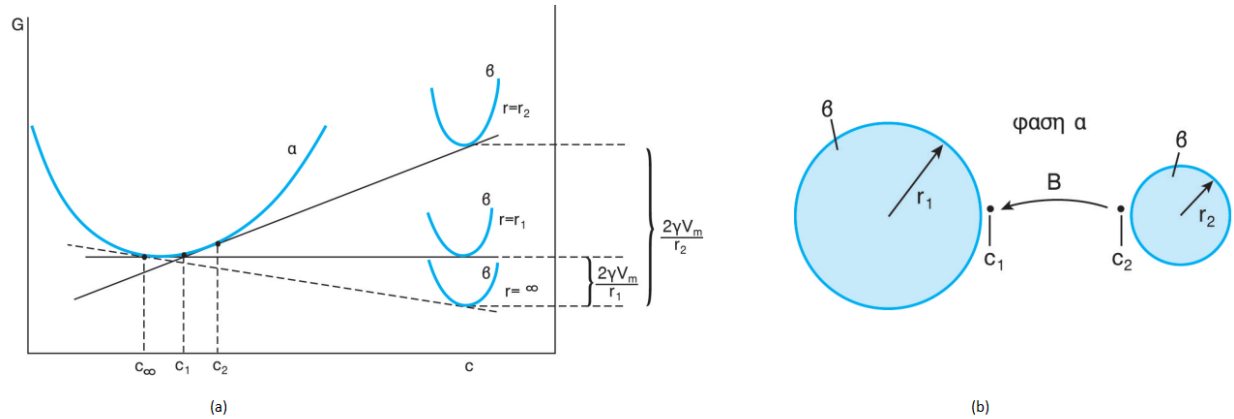

Figure 2.6: (a) Free energy – concentration of α and β phase diagram, for various values of curvature radius of β phase particle, (b) diffusion of B atoms from small to big particle. [4]

In 1956, Greenwood, studying the kinetics of coarsening, managed to express the rate, with which the radius of the precipitates increases. This rate, which can also represent the coarsening rate, is given by the equation 2.7, where $\bar{r}$ stands for the mean radius of the dispersion, the D for the diffusional coefficient, and the c_∞ to the concentration of α phase when the radius tends to infinity [4].

$$\frac{dr}{dt} = Dc_\infty \frac{2\gamma V_m}{kT} \frac{1}{r}\left(\frac{1}{\bar{r}} - \frac{1}{r}\right) \qquad 2.7$$

The graphical illustration of this correlation is given in Fig.2.7 for two different values of mean radius. By observing one curve in the graph, it occurs that for radius smaller than the mean radius value, the coarsening rates take negative values. This means, that in this case the precipitates shrink by losing solute atoms. Respectively, for precipitates with larger radius than the mean one, the coarsening rates are positive, and hence the precipitates coarsen by getting enriched in solute. The highest rate that a precipitate can grow during coarsening occurs when its radius is twice the mean radius of the dispersion [4].

Another expression of coarsening kinetics is called LSW theory and describes the variation of the mean radius of dispersion. The LSW theory is named after its investigators, Lifshitz, Slyozov and Wagner and can express the distribution of the particles' radius after the coarsening process. This theory's expression is given by the equation 2.8, according to which, the highest rates are given for precipitate radius equal to $1.13\bar{r}$ while the maximum size of a precipitate is $1.5\bar{r}$.

$$\bar{r}^3 - \bar{r_0}^3 = \frac{8D\gamma V_m c_\infty}{9kT} t \qquad 2.8$$

The term $\bar{r_0}$ stands for the mean distribution radius before coarsening starts. As the equation 2.8 shows, the coarsening rate depends on the diffusional coefficient as well as the concentration c_∞, which both increase with increasing the temperature. Thus, the coarsening process is very fast at high temperatures [4].

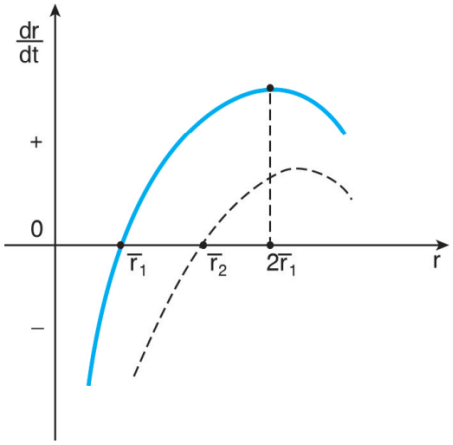

Figure 2.7: Coarsening rates as a function of radius for two different mean radius values, according to the Greenwood kinetics [4].

2.4 Precipitation Hardening Mechanisms

The mechanisms with which the dislocations slide is prevented during the precipitation process, can be expressed by the hardness evolution over aging time. A factor that affects the hardening mechanism is the coherency rate of the particles. In the initial stages of aging, the most precipitates are coherent phases. Coherent particles are considered penetrable to dislocations' movement, i.e., a dislocation can slide through them. However, because of the high strains which accompany the coherent precipitates, an intense stress field is created around them. These stress fields impinge with the stress fields of dislocations. This impingement obstructs the dislocation slide, and thus, also increases the hardness of the material. This increase can be computed by the following mathematical relationship (2.9) [4].

$$\Delta\tau = k_1 f^{1/2} r^{1/2} \qquad 2.9$$

Where k_1 is a constant, f is the volume fraction and r is the mean size of the precipitates. Another case that coherent precipitates contribute to the increase of hardness is the case of an ordered structure of penetrable particles. In this case an antiphase boundary (APB) on the dislocation's slide plane is created by the dislocation, that moves into the precipitate. The APBs present high interfacial energy, and hence, their contribution to the resistance of dislocations slide is significant. This contribution is expressed by the equation 2.10.

$$\Delta\tau = k_2\, \gamma_{APB}^{3/2}\, f^{1/3} r^{1/2} \qquad 2.10$$

Where γ_{APB} stands for the interfacial energy of APB. However, this kind of impingement is considered small ranged [4].

In later stages of precipitation, most of the precipitates are semicoherent or incoherent phases. This kind of precipitates are considered impenetrable to dislocations. Nevertheless, dislocations can surpass impenetrable precipitates by the Orowan mechanism. In this mechanism, a couple of adjacent precipitates can be considered as a Frank-Reed source. Similarly with the Frank-Reed mechanism, the sliding dislocation bends among an order of precipitates. As the dislocation bends around the precipitates, like in Fig.2.8., its points A and B obtain opposite sign and neutralize each other, creating this way a dislocation loop [4,5]. If the distance between the precipitates is L the maximum stress, required for a dislocation to surpass them, is equal to:

$$\tau_{max} = \frac{\mu b}{L} \qquad 2.11$$

However, due to the creation of loops, the distance L reduces, and the dislocations need more stress to surpass the particles. Because of this increase in the required stress, strain hardening takes place. This kind of strengthening is called Orowan hardening and can be expressed by the equation 2.12. Where k_3 is constant [4].

$$\Delta\tau = k_3 f^{1/2} r^{-1} \qquad 2.12$$

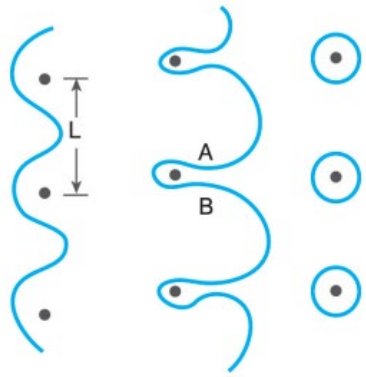

Figure 2.8: A dislocation's surpassing impenetrable precipitates by the Orowan mechanism[4]

In conclusion, the strengthening clearly depends on the size of the precipitates. Assuming a common axes for the mean precipitates' size and the aging time, the strengthening can be illustrated as a function of them, as Fig.2.9 shows. As it appears, in the initial stages of precipitation, the hardness increases proportionally to $r^{1/2}$, because of coherency strengthening. After a critical size (or time) the precipitates are considered impenetrable, and thus, the Orowan strengthening dominate, increasing the hardness proportionally to r^{-1}. The maximum hardness occurs, when the strengthening mechanism changes from coherency's to Orowan's [4].

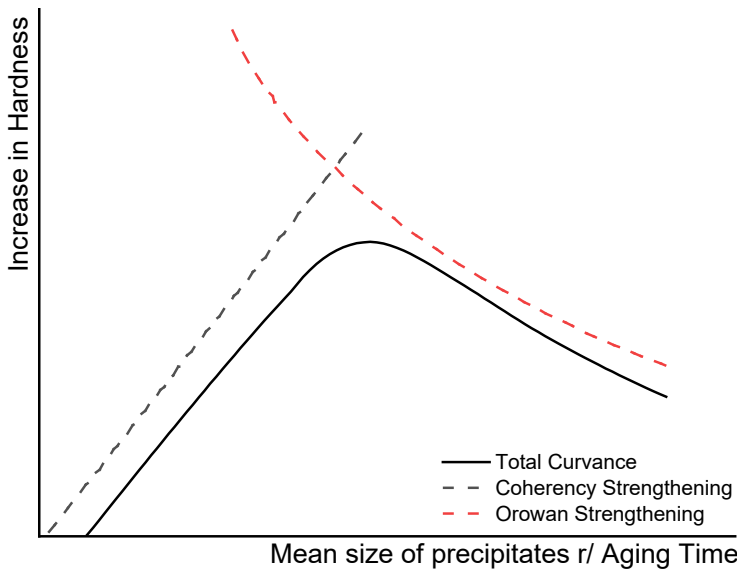

Figure 2.9: Strengthening as a function of the mean size of precipitates or aging time [4].

2.5 Precipitation in 7xxx series aluminum alloys

Many years now, the precipitation of the 7xxx aluminum alloys is a subject of many investigations because of the high strengthening potential they present and the complex mechanisms that govern this transformation. However, some phenomena such as the morphologies of the precipitate phases and their transition relationships are still controversial subjects for the scientific community. A review of the precipitation phases and their transformations in Al-Zn-Mg-Cu alloys follows in the next paragraphs.

2.5.1 Precipitation Sequence in 7xxx aluminum alloys

As every series of the heat treatable aluminum alloys, 7xxx series presents a characteristic precipitation sequence, i.e., a transition sequence of metastable and equilibrium phases, that occurres because of the coherency loss effect. The most acknowledged sequence for Al-Zn-Mg alloys, is [9,15–20]:

$$SSSS \rightarrow GP\ zones \rightarrow \eta'\ (metastable\ phase) \rightarrow \eta\ (equilibrium\ phase)$$

The presence of T and its precursor T' has been also reported in many studies [9,21,22], suggesting various sequences as the following two:

$$\begin{cases} SSSS \rightarrow GP\ zones \rightarrow \eta'(metastable) \rightarrow \eta(MgZn_2) \\ SSSS \rightarrow T'(metastable) \rightarrow T \end{cases}$$

$$SSSS \rightarrow G.P.zones \rightarrow \eta' + T'(metastable\ phases) \rightarrow \eta + T\ (equilibrium\ phases)$$

According to most of the studies the main hardening phase is the η' metastable phase [18,20,23,24], while some studies consider also the contribution of the GP zones and the metastable T' to the total hardening [21]. These variations may depend on the chemical compositions of the alloys, for example the T' is considered the dominant hardening phase on alloys with low Zn/Mg ratios, while η' dominates at higher ratios [20].

2.5.1.1 GP zones

The full name of these zones, Guinier-Preston zones, originates from the two metallurgists Guinier and Preston, who were the first to identify them through their independent work in aluminum alloys, in 1938 [25]. They are considered the first metastable nuclei responsible for hardness increase, and they are in complete coherence with the aluminum matrix.

In the Al-Zn-Mg-(Cu) alloys, GP zones present spherical shapes and their size can vary from 1nm in the initial stages of natural aging to 9nm [19,26–28]. Investigations in their composition report a Zn:Mg ratio in the range of 1.0 to 1.5 [27,28]. The formation of GP zones seems to derive from the combination of zinc- and magnesium -vacancy rich clusters to Zn-Mg clusters which act as their nucleation sites [18,21,24]. Furthermore, on the one hand, in alloys with concentrations in magnesium lower than 0.9%, the migration of zinc and magnesium VRCs control the growth of GP zones. On the other hand, in alloys with higher concentrations, only the magnesium VRCs migration is responsible for the zones' growth [21,29].

A still controversial theory about the GP zones in Al-Zn-Mg-(Cu) alloys, is the existence of a second type of zones. Through their investigation in Al-Zn-Mg alloys precipitation by small-angle X-ray scattering (SAXS), in 1958, Schmalzried and Gerold were the first to find indications about the existence of a second temperature dependent GP zone type, with alternating zinc and magnesium {001} planes. In their study, they also observed an internal order in GP(I) type suggested to be based on the Cu-Au(I)

type of ordering. [12,18,30] Similar evidence occurred by the later investigations of Dlublek et al, in 1983 through their positron study. According to their observations, the first type, GP(I) zones are the same type of zinc-rich and vacancy-free zones that form in the binary Al-Zn alloys. On the contrary, vacancies were presented in GP(II) zones, probably due to the contained magnesium atoms [31]. In a later study, in 1986, Dlublek et al supported that a transformation process takes place between the two types of zones at room temperatures and after quenching. According to this hypothesis, pairs of zinc atoms and vacancies, which obtain high mobility even at room temperatures, form GP(I) zones. Because of the strain field created by the GP(I) zones, magnesium atoms are allowed to diffuse towards these zones, forming this way the GP(II) zones. Therefore, alloys containing high concentrations of magnesium are expected to contain a higher density of GP(II) zones than of GP(I) zones [32]. On the other hand, other investigators supported that GP(II) zones nucleate on vacancy rich clusters, formed simultaneously with GP(I) zones at room temperatures [19,33].

The existence of a second type of zones in this aluminum alloys series, is also supported by more recent studies. As an example, in their electron diffraction study, Berg et al in 2001, reported that the formation of the first type occurred at low temperatures, in the range of room temperature to 140-150°C, while the second type was observed after quenching from temperatures above 450°C and aging above 70°C. The electron diffraction results showed GP(II) zones on $\{111\}_{Al}$ planes as zinc-rich planar sheets. In addition, internal ordering was observed in GP(I) zones, in accordance with Schmalzried and Gerold's results [18]. According to bibliography, GP(I) zones have been identified as spherical particles with a diameter of 2-3 nm, on $\{001\}_{Al}$ planes [24], while GP(II) are considered disc like particles of 1-6 atomic layers thickness and 3-6nm width parallel to $\{111\}_{Al}$ planes [15].

2.5.1.2 Reversion of GP zones and Nucleation of η'precipitates

In the early stages of artificial aging, a rapid decrease in hardness and in volume fraction of GP zones due to the dissolution of GP zones has been observed by several investigators [7,12,19]. This phenomenon is called reversion and can be distinguished in partial and total, depending on whether the dissolution of GP zones and the nucleation of η' are simultaneous procedures or not [12].

In cases of total reversion, the GP zones dissolve completely before the nucleation of η' starts. As a result, the values of hardness and volume fraction after the dissolution, reach the respective as-quenched values. Even the large but temporal decrease in hardness, treatments during which complete reversion occurs, such as duplex aging, result in finer η' dispersions. The dissolution of GP zones leaves behind intense local fluctuations in concentrations of zinc and magnesium. These enriched in solute regions are considered to act as preferable nucleation sites for η' precipitates [12].

When the dissolution of GP zones is overlapped by the nucleation of η', the hardness is partially decreased, and different transformation mechanisms take place. There are different assumptions about the nucleation of η' in partial reversion cases. Some authors support that η' nuclei form directly from overcritical GP zones, while others believe that coexisting VRCs or η' nuclei evolve to the metastable η' phase [12].

The assumption that VRCs act as nucleation sites for η' is supported by the fact that even in short aging times, insufficient for GP zones formation, η' particles have been observed. According to Ryum and Katz, at aging temperatures above the solidus line of GP zones, VRCs are the only possible nucleation sites for η', while below the solidus, both GP zones and VRCs can act as nucleation sites. However, VRCs seem be the dominant nucleation sites only for short times and in low concentrated alloys (< 2.5% in zinc, and < 2 in magnesium) [12].

In duplex aging, the GP zones formed in the first step are considered stable enough to act as the dominant nucleation sites for η' precipitates, while in one-step aging, η' precipitates nucleate heterogeneously in grain boundaries, dislocations and dislocation loops. Another theory about the nucleation of η' during duplex aging is that in the second stage, η' particles nucleate directly from the stable GP(II) zones, while the GP(I) zones, unstable in these temperature ranges, dissolve [12].

2.5.1.3 η΄ metastable and η equilibrium phase

The metastable η' phase is considered as one of the main hardening phases in 7xxx series. Its precipitates take the form of thin platelets on $\{111\}_{Al}$ planes [19,27]. Their width varies from 5 to 10nm, while their thickness from 3 to 4nm [15]. There are several suggestions about the structure and the composition of the η' phase. According to Gjonnes and Simensen η' structure is orthorhombic with lattice parameters α = 0.496nm and c = 1.403nm [12,34]. Another structure model suggested for η' phase by Li et al., is a hexagonal structure of $P\bar{6}$ group with the same parameters (α = 0.496nm and c = 1.403nm). This model contains eight symmetry-inequivalent sites: the six sites are occupied by three couples of Al, Zn, Mg atoms respectively, and the other two can be occupied either by Zn or by Al [12,35]. The most recognized model was suggested by Auld and Cousland. According to them, the η' particles have hexagonal structure of $P\bar{6}m2$ group. The model contains eight symmetry-inequivalent sites: two of them are fully occupied by zinc and other two by aluminum atoms. Other two sites are occupied half by zinc and half by aluminum, while in the rest two sites, the one-third is occupied by vacancies and the two-thirds by zinc [34]. The stoichiometry that results by this model is $Mg_4Zn_{11}Al$, different from the generally accepted composition $MgZn_2$ [12,34]. Also, Kverneland et al. suggested a composition of $Mg_4Zn_6Al_{8-x}$ where x represents the number of vacancies included in the phase [23].

The equilibrium phase η presents a rod-like shape with a size in the range of 15-30nm and numerous orientation relationships with the matrix. Its structure is hexagonal with parameters α = 0.5225nm and c = 0.8568nm [15,21,36]. Numerous orientation relationships of η with the aluminum matrix have been observed [36]. Some of the reported orientations are presented in table 2-2. The η_2 type is considered the successor of η' because of their similarity in shape and orientation relationships. The η_1 type forms in conditions that η cannot, and its precipitation seems to occur directly from the matrix [36]. The composition of η phase is generally considered as $ZnMg_2$. However, some studies report that η is isomorphus to $MgZn_2$ and AlCuMg, and its true composition is expressed as $MgZn_{2x}Al_{1-x}Cu_{1-x}$ where x is parameter for the deviation from $MgZn_2$ [37].

Orientation relationships between the η-precipitates and the aluminum lattice
$(10\cdot 0)_{\eta_1} \parallel (001)_{Al};\ (00\cdot 1)_{\eta_1} \parallel (110)_{Al}$
$(00\cdot 1)_{\eta_2} \parallel (1\bar{1}\bar{1})_{Al};\ (10\cdot 0)_{\eta_2} \parallel (110)_{Al}$
$(00\cdot 1)_{\eta_3} \parallel (1\bar{1}\bar{1})_{Al};\ (11\cdot 0)_{\eta_3} \parallel (110)_{Al}$
$(00\cdot 1)_{\eta_4} \parallel (110)_{Al};\ (12\cdot 0)_{\eta_4} \parallel (1\bar{1}\bar{1})_{Al}$
$(\bar{1}2\cdot 0)_{\eta_5} \parallel (1\bar{1}\bar{1})_{Al};\ (30\cdot 2)_{\eta_5} \parallel (110)_{Al}$
$(\bar{1}2\cdot 0)_{\eta_6} \parallel (1\bar{1}\bar{1})_{Al};\ (20\cdot 1)_{\eta_6} \parallel (1\bar{1}2)_{Al}$
$(\bar{1}2\cdot 0)_{\eta_7} \parallel (1\bar{1}\bar{1})_{Al};\ (10\cdot 4)_{\eta_7} \parallel (110)_{Al}$
$(\bar{1}2\cdot 0)_{\eta_8} \parallel (1\bar{1}2)_{Al};\ (00\cdot 1)_{\eta_8} \parallel (31\bar{1})_{Al}$
$(\bar{1}2\cdot 0)_{\eta_9} \parallel (001)_{Al};\ (00\cdot 1)_{\eta_9} \parallel (110)_{Al}$

Table 2-2: Orientation relationships between the η-precipitates and the aluminum lattice [36].

2.5.1.4 T' metastable and T equilibrium phases

The presence of T and its precursor T' has been reported in alloys with higher Mg:Zn ratio [9,22]. According to a recent study, alloys with low concentrations in zinc are strengthened by T' precipitates, while in alloys with higher zinc concentrations both η' and T' are responsible for the material's strengthening [20]. The precipitation of T' and T is a thermally activated procedure, i.e., T' and T precipitates form at higher aging temperatures [7,21]. The structure of both precipitates is bcc with parameters α = 1.416nm for T and α = 1.44 to 1.45nm for T'. They also share the same orientation relationship with the matrix, $(100)_T, \parallel (111)_{Al}$ and $(010)_T, \parallel (11\bar{2})_{Al}$ [22]. The only difference between them, it is their chemical composition. The stable composition of the equilibrium T phase can be expressed as $Mg_{32}(Al, Zn)_{49}$ [22]. On the other hand, the metastable phase T' presents a coring phenomenon in their composition. Specifically, they are composed of a large magnesium and zinc-rich core, and layers with lower magnesium content [22]. As the T' precipitates grow, they are getting enriched with zinc and magnesium until they reach the composition of the equilibrium T phase, indicating the close relationship between their size and their composition [20].

2.5.1.5 Effects of copper addition in the 7xxx series alloys' precipitation

Aluminum alloys of 7xxx series with small copper additions seem to have greater strengthening potentials than the Al-Zn-Mg alloys [1,3,24]. The upper limit of copper concentration, that can result in higher peak hardness, is reported to be 3%. For higher concentrations, copper seem to have the opposite effects in precipitation hardening [24]. The quaternary Al-Zn-Mg-Cu alloys have better response in natural and in one-step aging, while duplex aging seem to result in lower peak hardness with respect to one-step aging [1]. Thus, it is of high importance to understand how a small addition of copper can affect the precipitation phenomena of these alloys.

According to studies, copper does not change the transition sequence of the Al-Zn-Mg alloys, however it stabilizes the GP zones at higher temperatures, and decrease the formation temperature of η', making the transition of GP zones to η' smoother [1,3,23,24]. The better response of copper containing alloys to one step aging, as well as the enhancement of rapid precipitation in the early stages of aging, may occur due to the increased number of VRCs because of the interaction of copper with quenched-in vacancies [1]. Copper increases also the number of GP zones by forming more Cu containing ellipsoidal GP zones in addition to the Cu-free spherical zones. The shape of the zones that contain copper is probably due to the strain that copper atoms introduce to the particle's structure [1]. Except of retarding the dissolution of GP zones, copper seem to retard also the growth and the coarsening of the precipitates. An explanation of this effect may be that magnesium and copper form very stable complexes, which are difficult to diffuse [3]. Finally, the higher supersaturation, caused by the copper addition, leads to smaller nucleation radius for all precipitates [3].

2.5.2 Effect of Zr and Cr additions on microstructures of 7xxx series alloys

In many cases, aluminum alloys of 7xxx series may contain little amounts of chromium and zirconium. These additions are usually applied to improve some mechanical properties, such as strength, ductility and fracture toughness of the material [38]. These elements tend to form precipitates in the aluminum matrix, called dispersoids, during homogenization and quenching of the material [7,37–39]. Even dispersoids can inhibit the recrystallization, they usually act as preferable nucleation sites for non-hardening η phase particles [39]. The most identified types of such particles in 7xxx series alloys are the chromium containing dispersoids such as $Al_{18}Mg_3Cr_2$ and the zirconium containing Al_3Zr. The chromium containing dispersoids are extremely efficient nucleation sites for heterogeneous precipitation during aging. On the contrary, Al_3Zr seem to transfuse lower quench sensitivity and fine

grain sizes to the material. Therefore, zirconium additions are industrially preferred rather than chromium [7,33,39].

The usual size of Al_3Zr dispersoids varies from 15 to 25nm [7,38], and their equilibrium structure, called β, is quadratic with parameters α = 0.43nm and c = 1.69nm [37]. However, most of the times the dispersoids are observed in the form of the β precursor. These particles present cubic L_{12} structure [7,37,38], and are usually considered coherent with the aluminum matrix, due to their small size and misfit [7]. The nucleation of η' precipitates that occurs on Al_3Zr dispersoids, leads to the formation of η' precipitates bands in the aged alloy [38]. These precipitates have also some positive effects in the strengthening process. Firstly, they can also contribute to the strengthening of the material by the Orowan's and substructure's strengthening mechanisms [38]. Furthermore, the growth and the coarsening of these dispersoids are activated only at high temperatures (above 450°C) because of the low diffusional coefficient of zirconium [37].

The $Al_{18}Mg_3Cr_2$ is a common chromium containing dispersoid and is also reported as E phase. E phase forms during homogenization and presents lath or tetragonal shapes. The size of these particles ranges from 100 to 200nm, much larger that the Al_3Zr dispersoids. During quenching, these dispersoids act as efficient nucleation sites for heterogeneous precipitation of η phase, depleting significantly the matrix of solute and vacancies. As a result of this depletion, the strength potentials of the material are reduced [39].

2.6 Modeling of precipitation in 7xxx alloys

Predicting the precipitation behavior of heat treatable alloys via simulation models, could be an important tool for digital alloy and process design. The last years, many investigations have been conducted on this subject and multiple simulation models with good accuracy have been proposed. The most known is the approach of the Kolmogorov-Mehl-Avrami (KJMA) theory. Some characteristic variables such as PSD (Precipitate Size Distribution) are usually used in order to define the precipitation microstructure of the alloys. Specifically, PSDs are used by the Langer-Schwartz (LS) approach to express the evolution of precipitation [40]. An extension of this theory is the Kampmann-Wagner (KWN) numerical model [41]. The KWN model discretizes the PSD into classes of size, and solves the continuity PSD equation directly, describing efficiently the precipitation kinetics [40,41]. Many modifications of the KWN model have been developed to extend it for multicomponent and multiphases' alloys. In their recent study, Herrnring et al., applied the KWN in an Al-Zn-Mg-Cu alloy assuming the metastable η' phase as the only precipitation product. In combination with SAXS experiments, they achieved results with good accuracy [40]

Chapter 3 Methodology

3.1 Material Studied

The alloy that was used for this thesis' purposes is the aluminum alloy of the 7xxx series, AA7075. The limits of the chemical composition of its alloying elements according to ASM Handbook Committee are presented in the Table 3.1. In extruded products, a small amount of zirconium and titanium (Zr+Ti), in the maximum limit of 0.25 wt%, may be also contained [2]. The material was received as a sheet metal.

Material	Zn	Mg	Cu	Si	Fe	Mn	Ti	Cr
AA7075 (wt%)	5.1-6.1	2.1-2.9	1.2-2.0	0.40	0.50	0.30	0.20	0.18-0.28

Table 3-1: Chemical composition of the aluminum alloy 7075 according to ASM Handbook Committee [2]

3.2 Experimental Procedures

The main experimental procedures that took place during this thesis, in order to gain more information about the alloy's microstructure and its response at aging heat treatment, were a metallography and hardness measurements after various aging treatments. In the following subsubsections of the chapter, the steps, followed for these procedures as well as the preparation of the specimens will be analyzed.

3.2.1 Preparation of specimens

For its examination, the as received metal sheet was cut in rectangular specimens of 1cm length and 0.5cm width. The cutting was processed with Struers silicon carbide cut-off wheels and water cooling. Further preparation was required for the metallographic examination. Firstly, the specimens were mounted into epoxy resin cylinders. For a smooth surface, grinding and polishing processes followed. Grinding was performed in five stages, with silicon carbide abrasive paper, as the ASM Aluminum Committee suggests. Specifically, the applied grits were: 220, 400, 600, 800, 1000. At all stages, as suggested, running water was used to lubricate the surfaces, and avoid the temperature increase. Polishing was performed in two stages. In the first stage, diamond paste of 1μm was applied in a short-nap cloth, at the presence of water-based lubricant. In the second stage, powder of alumina (Al_2O_3), dissolved in distilled water, was used to polish the specimens on a billiard cloth. A modified chemical Keller's etchant was finally applied to the specimens for a few seconds, in order to achieve observing the grain boundaries. The contents of the etchant were 10mL HNO_3, 1.5mL HCl, 1.0mL HF and 87.5mL of water. After the etching, the specimen were washed with water and alcohol and drained with hot air [42].

3.2.2 Metallography

The metallography was performed using the Leitz Aristomet optical microscope. Three specimens were used in their as-received state, for the examination of the three characteristic planes for the rolling process, i.e., the rolling surface and the side surfaces. The scheme in Fig 3.1 adds labels to these surfaces for easier reading of this thesis. Thus, the LT plane will correspond to the rolling face, the ST to the side surface perpendicular to the rolling direction, while the LS plane to the side surface parallel to the rolling face.

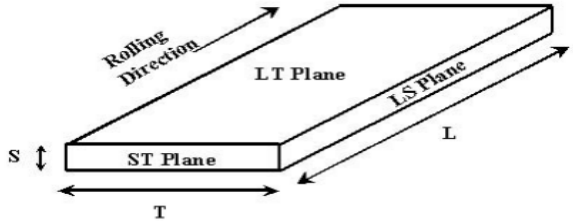

Figure 3.1: Labelling Scheme, LT plane: rolling surface, ST plane: perpendicular to rolling direction, and LS plane: parallel to rolling direction

3.2.3 Aging Heat Treatments

All the specimens were applied at a solution treatment at 480°C for 1hr, and then quenched into cold water. For the purposes of this experiment, after the quench, the specimens were kept into refrigeration to stall any precipitation process. Four different aging treatments were performed, a one-step aging and three duplex agings. The one-step aging was performed at 160°C, as applied at a AA7075 alloy in the study by Yang et al. [43]. For the duplex treatments the study of Emani et al. was chosen as reference [17]. The first treatment, similarly with the study, was a pre-aging at 120°C for 55min and then aging at 180°C until peak hardness was reached. Two others duplex agings were followed, trying to test the alloy's response at less aging time of pre-aging and at lower temperature in the final step. Specifically, one treatment of 20min pre-aging at 120°C and aged at 180°C, and another of 55min pre-aging at 120°C but then aged at 160°C took place.

3.2.4 Microhardness Measurements

The microhardness measurements were taken by using a Wilson Instrument 402 MVD Vickers and Knoop Tester. The testing was processed in Vickers scale, with a load of 200gr. For every heat treatment, several measurements were performed for variant aging times, in order to find the peak hardness. The Table 3.2 below presents the aging times of the measurements for every aging treatment. In addition, a measurement was taken immediately after the quench process. Every measurement was performed by taking six different values from different regions of the examined specimen and computing their mean value. For the presentation of the microhardness results, the OriginPro 2019b [44] software was used to plot the microhardness as a function of aging time for every heat treatment.

One-step Aging	Pre-aging	Duplex Aging		
at 160°C	at 120°C	After 55min at 120°C and then at 180°C	After 30min at 120°C and then at 180°C	After 55min at 120°C and then at 160°C
(hours)	(minutes)	(minutes)	(minutes)	(minutes)
1.5	30	5	5	15
4	55	10	15	30
6		15	30	45
8		25	60	60
12		60	90	75
16		90	120	90
18		120	150	105
20				120
24				135

Table 3-2: The aging times for microhardness measurements for every heat treatment

3.3 Modeling Precipitation with numerical model KWN

In the purpose of studying the microstructure phenomena and the strengthening evolution of the 7075 aluminum alloy during precipitation, the applied heat treatment of one step aging was simulated through the TC-PRISMA Precipitation Module. This module is based on the Langer-Schwartz theory and uses the Kamppman-Wagner numerical model for its calculations. The TC-PRISMA precipitation module by collaborating with the calculating tools of Thermo-Calc and the Diffusion Module (DICTRA), obtains all the required quantities for KWN model calculations, without the danger of inaccurate assumptions. The thermodynamic and mobility data, required in this simulation were received from the Thermo-Calc databases TCAL7 and MOBAL5.

3.3.1 KWN methodology

The KWN model describes the precipitation kinetics by decreasing the system's Gibbs energy via the nucleation and growth mechanisms in order to approach a mass equilibrium state. This model solves directly the continuity equation of the PSD's evolution over time, by discretizing the PSD into size classes. If f stands for the PSD, v(r) for the growth rate of a particle with r radius, and j(r) for the distributed nucleation rate, the continuity equation of the PSD can be expressed as:

$$\frac{\partial f}{\partial t} + \frac{\partial}{\partial r}[v(r)f(r)] = j(r) \qquad 3.1$$

The term of distributed nucleation rate $j(r)$ can be defined by the following equations:

$$I(t) = \int_{r_c}^{\infty} j(r)dr \qquad 3.2$$

Where r_c represents the critical radius for nucleation and $I(t)$ the nucleation rate for multicomponent systems based on the classical nucleation theory:

$$I(t) = NZ\beta^* \exp\left(-\frac{16\pi}{3}\frac{\gamma^3 V_m^2}{\left[\Delta G_m^{\alpha\to\beta}\right]^2 k_\beta T}\right)\exp\left(-\frac{\tau}{t}\right) \qquad 3.3$$

Where γ is the interfacial energy, the V_m is the molar volume of the precipitated phase, τ is the incubation time for establishing steady nucleation rate conditions, and k_β is the Boltzmann's constant. The term $\Delta G_m^{\alpha\to\beta}$ expresses the maximum driving force for the transformation of α to β phase. The Zeldovich factor Z is determined by the respective equations:

$$Z = \frac{V_m}{2\pi N_A r^{*2}}\sqrt{\frac{\gamma}{k_\beta t}} \qquad 3.4$$

Where N_A is the Avogadro number and $r^*$is the critical radius for nucleation expressed by the equation:

$$r^* = -\frac{2\gamma V_m}{\Delta G_m^{\alpha\to\beta}} \qquad 3.5$$

The atomic attachment rate β^*can be expressed as:

$$\beta^* = \frac{4\pi r^{*2}}{\alpha^4}\left[\sum_i \frac{\left(X_i^{\beta/\alpha} - X_i^{\alpha/\beta}\right)^2}{X_i^{\alpha/\beta} D_i}\right]^{-1} \qquad 3.6$$

Where α is the lattice parameter, $X_i^{\beta/\alpha}$ and $X_i^{\alpha/\beta}$are the mole fractions of component i at the interface between the precipitate and matrix, respectively.

For calculating the growth rate, the simplified model available and suggested by the precipitation module was applied. According to this pseudo-steady state model, the growth rate can be calculated by the subsequent equations:

$$v(r) = \frac{K}{r}\left[\Delta G_m - \frac{2\gamma V_m}{r}\right] \quad 3.7$$

Where K is defined as:

$$K = \left[RT\sum_i \frac{X_i^{\beta}(r) - X_i^{a}(r)}{X_i^{a}(r)M_i}\right]^{-1} \quad 3.8$$

In equation 3.4, the term ΔG_m represents the driving force for nucleation of the precipitated phase. In the equation 3.5, R stands for the gas constant, T for the temperature, M_i is the atomic mobility of the i component, while X_i^a and X_i^{β} are the mole fractions of the matrix and the precipitate's phase respectively.

In every time step of the module's calculations, the concentration of the matrix is recalculated via a mass balance equilibrium, resulting in a complex non-linear equation. To solve this equation the precipitation module TC-PRISMA applies the numerical method of characteristics. According to this method, the number of particles in every size class of the discretized continuity equation, changes only with the nucleation of same size particles.

3.3.2 Modeling the experiment of one-step aging with TC-PRISMA Precipitation Module

The experiment of one-step aging at 160°C was selected to be simulated via Precipitation Module (TC-PRISMA). In the first attempt to approach the experimental results, the η'metastable phase was assumed as the only hardening phase. In the second approach, both η' metastable and η equilibrium are considered to contribute to the strengthening of the material. In the database TCAL7, the η' phase is presented as ETA_PRIME, while the equilibrium η phase as C_14 LAVES. The precipitate of η' phase was assumed to present plate shape with an aspect ratio (i.e., the fraction of larger diameter to the smallest one) equal to 2.3 [15]. On the other hand for η equilibrium, the needle shape was selected with an aspect ratio 2.5 [45].

Provided that the accurate chemical composition of the studied aluminum alloy was not identified, various compositions in the range of the suggested concentration limits in AA7075, were applied. In table 3-3, all the applied chemical compositions are presented. According to KWN model, the various compositions are expected to affect the nucleation rate through the atomic attachment rate β^*, as well as the growth rate through the K factor.

Since the initial material's state in the simulation is the as-quenched state, multiple values for the prefactor of the mobility enhancement were applied to approach the required time for peak hardness. This prefactor multiplies to the mobility data of the calculation and scales the mobility by a certain amount. Interfacial energy values for the two phases were found in the bibliography and applied in the approach 2. The interfacial energy of η' phase was reported equal to 0.06 J/m^2, while this of the equilibrium η phase was equal to 0.2 J/m^2 [45]. The simulation aging time was considered equal to 108.000 seconds (=30 hrs.). The microhardness values were calculated by the simplified yield strength model. For further study of the precipitation phenomena, except of the microhardness evolution, other characteristic quantities were calculated by TC-PRISMA module. Specifically, these quantities

were PSDs, mean and critical radius of precipitates, volume fractions of phases and their composition, as well as nucleation rates.

Various Chemical Compositions of AA7075 (% w/w)			
Applied in approach 1		**Applied in approach 2**	
Al-5.6Zn-2.5Mg-1.6Cu	Al-5.6Zn-2.5Mg-1.2Cu	Al-5.1Zn-2.1Mg-1.2Cu	Al-5.8Zn-2.5Mg-1.6Cu
Al-5.2Zn-2.5Mg-1.6Cu	Al-5.6Zn-2.5Mg-1.4Cu	Al-5.6Zn-2.1Mg-1.2Cu	Al-5.8Zn-2.3Mg-1.4Cu
Al-5.3Zn-2.5Mg-1.6Cu	Al-5.6Zn-2.5Mg-1.8Cu	Al-6.1Zn-2.1Mg-1.2Cu	
Al-5.8Zn-2.5Mg-1.6Cu	Al-5.6Zn-2.5Mg-2Cu	Al-5.1Zn-2.5Mg-1.2Cu	
Al-6.1Zn-2.5Mg-1.6Cu	Al-5.8Zn-2.1Mg-1.6Cu	Al-5.1Zn-2.9Mg-1.2Cu	
Al-5.6Zn-2.1Mg-1.6Cu	Al-5.8Zn-2.3Mg-1.6Cu	Al-5.1Zn-2.1Mg-1.6Cu	
Al-5.6Zn-2.3Mg-1.6Cu	Al-5.8Zn-2.5Mg-1.6Cu	Al-5.1Zn-2.1Mg-2Cu	
Al-5.6Zn-2.7Mg-1.6Cu	Al-5.8Zn-2.3Mg-1.8Cu	Al-5.8Zn-2.1Mg-1.2Cu	
Al-5.6Zn-2.9Mg-1.6Cu	Al-5.8Zn-2.3Mg-2Cu	Al-5.8Zn-2.3Mg-1.2Cu	

Table 3-3: The applied compositions of AA7075 to the Precipitation Module (TC-PRISMA)

Chapter 4 Results

4.1 Metallography

The rolling effect in the material's microstructure is obvious in the metallography Fig.4.1, Fig.4.2, Fig.4.3, Fig.4.4). In the side surfaces of rolling (Fig.4.1, Fig.4.4), the wrought structure, which is a result of rolling process, and characterized by a uniform distribution of elongated grains, can be observed. On the contrary, the rolling surface (Fig.4.2, Fig.4.3) presents non uniform grains of greater sizes, a structure associated with the initial state of the material (before the rolling process) [46]. The different color of the grains in the figures indicates their different orientation.

The size of the particles, presented as black spots in all the following figures, can vary from 1 to 11μm. The results of the optical microscopy are not sufficient to identify particles such as hardening phases. Therefore, because of their large size, they cannot represent any of the reported phases (hardening phases or the reported dispersoids), the maximum size of which do not surpass the 200nm. A study via an electron microscope could give more evidence for the particles' identity, such as the particles' chemical composition.

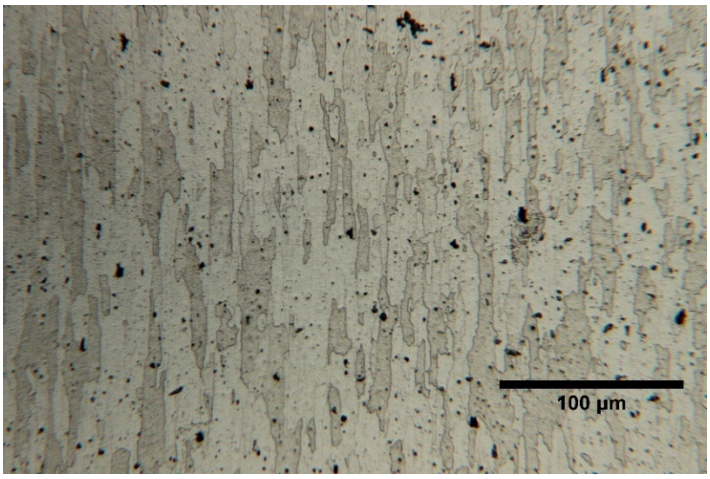

Figure 4.1: Uniform distribution of elongated grains and presence of dispersoids in ST plane (x200)

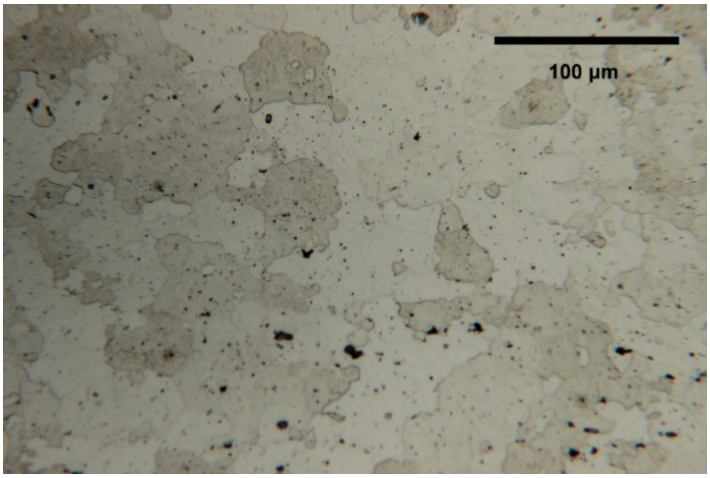

Figure 4.2: Big grains with disparate distribution and presence of dispersoids in LT plane (x200)

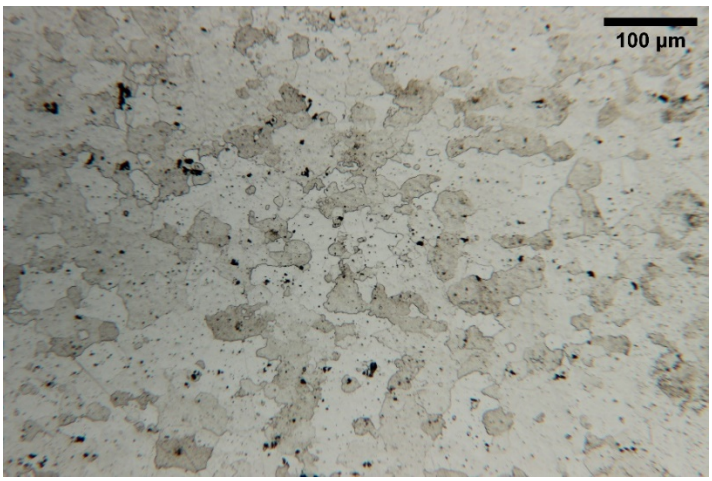

Figure 4.3: Big grains with disparate distribution and presence of dispersoids in LT plane (x100)

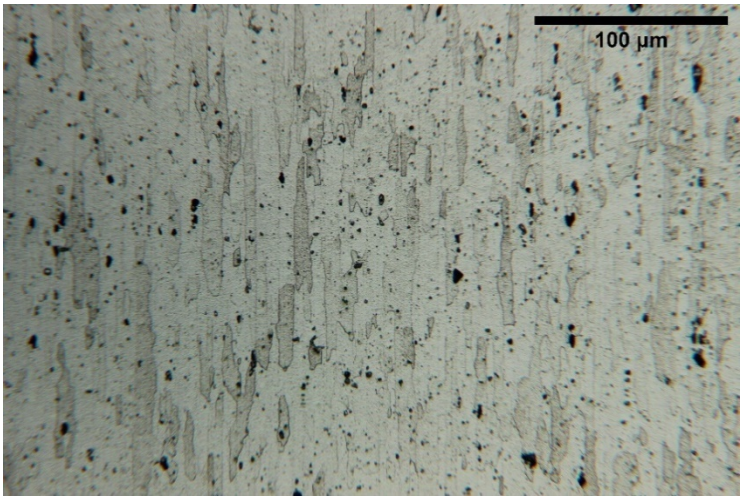

Figure 4.4: Uniform distribution of elongated grains and presence of dispersoids in LS plane (x200)

4.2 Microhardness Measurements

For a better presentation of the results, the measurements were plotted as a function of aging time for every heat treatment, as stated and previously. In the plots of Fig.4.6 and Fig.4.7, the mean value of the six hardness measurements for specific aging times are presented with their standard variation as the accuracy error. In the Figure 4.6, comparing the results of the one-step aging at 160°C of the studied alloy in this thesis, with the respective values of the Yang et al.'s study, shows that they are in good accordance. Even the variance of 10°C in their solution temperatures, the microhardness value of the as-quenched state was almost the same for both experiments, equal to 92.5 HV in the present study. The value of 191.9 HV at the peak hardness was also very close with the respective peak hardness, although it was reached in a longer aging period. Specifically, for the examined alloy, the peak was reached at 8 hours, while in the Yang's study was reached at 6 hours. A variation is also noted

in the hardness reduction rates during coarsening. These variations may occur due to slightly different alloy compositions.

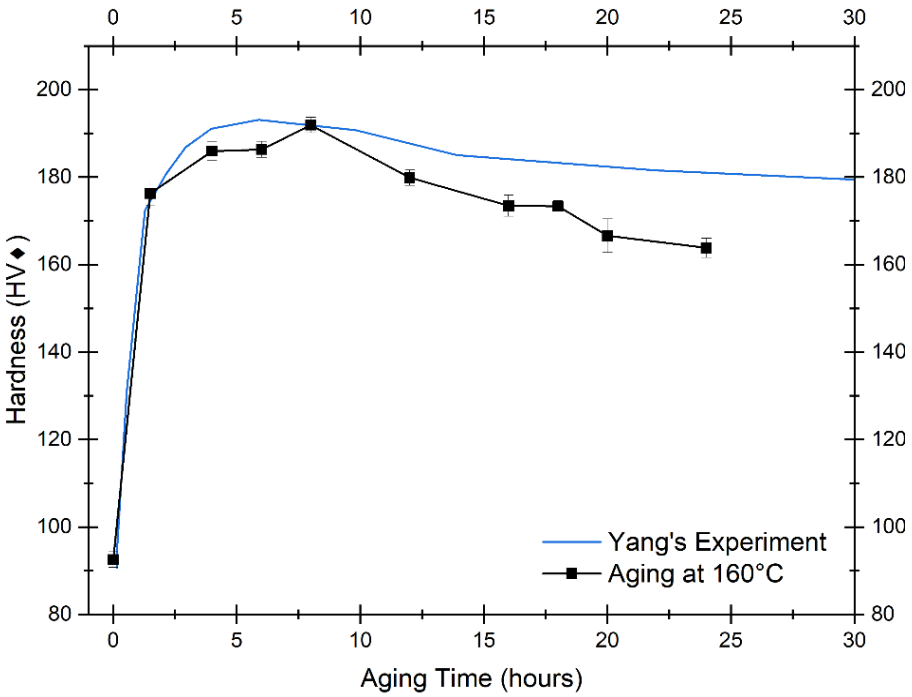

Figure 4.5: Microhardness evolution over aging time for a one-step aging at 160°C [43]

In Fig.4.6 the microhardness evolution over time during the second stages of the three duplex aging treatments, as well as the respective results of the Emani et al.'s study [17] are presented. The first aging step at 150°C for 55min seems to result in higher hardness (164.8HV) than the respective experiment of Emani et al. This deviation is probably caused by the different solution treatments applied. In this study a solution treatment for 1hr at 480°C was applied, while in the Emani's study the treatment lasted for 30min at 490°C. The shorter solution time may result in a lower rate of homogeneity, meaning lower supersaturation, and thus, lower driving force for precipitation. In the second aging step at 180°C, starting from higher hardness, the studied material reaches faster the peak hardness, the value of which is close to this of the corresponding experiment (192.1HV). Another reason for the different results of the two experiments, is that the specimens in Emani et al.'s study were water quenched after the first aging step, while for the purposes of this study the specimen were air cooled at room temperature. In addition, significant deviation is presented in the hardness reduction rates of the two experiments.

Worth to be noted that the peak hardness value of the duplex treatment (55min at 120°C and then at 180°C) is almost equal to the corresponding value of the one-step aging at 160°C but reached in extremely shorter aging period. This indicates the industrial benefits of the duplex aging because of the shorter required time. However, it comes in contrast with the reported information about the response of copper containing alloys to duplex aging treatments [1].

Both modifications of this duplex treatment, i.e., the first with shorter aging time (30min) in the first step, and the second with lower aging temperature (160°C) in the second step, give higher peak hardness but in longer aging periods. The former reaches the value 194.5HV at peak hardness in 30min of second step aging time, while the latter reaches the even higher value 203.8HV in 105min (1 hr. and 45min). The shorter time in the first aging, result in lower hardness (148.05HV) in the end of the step, closer to the corresponding value of the Emani's study. Additionally, as illustrated in the Fig.4.6, the

results of this experiment are in better accordance with the results of the Emani's study, rather than the results of the initial experiment. The hardness curve of the experiment with lower aging temperature in the second step, presents great interest because of the temporal reduction in hardness in the first 30 min of second step aging. According to bibliography, this reduction may occur due to partial reversion phenomenon, during which some unstable in higher temperatures GP zones, formed in the first aging step, dissolve in the initial stages of the second step, while others more stable GP zones transform to the hardening η' phase. In bibliography, the stable zones are linked with the GP(II) type of zones, while the unstable with the GP(I) [12].

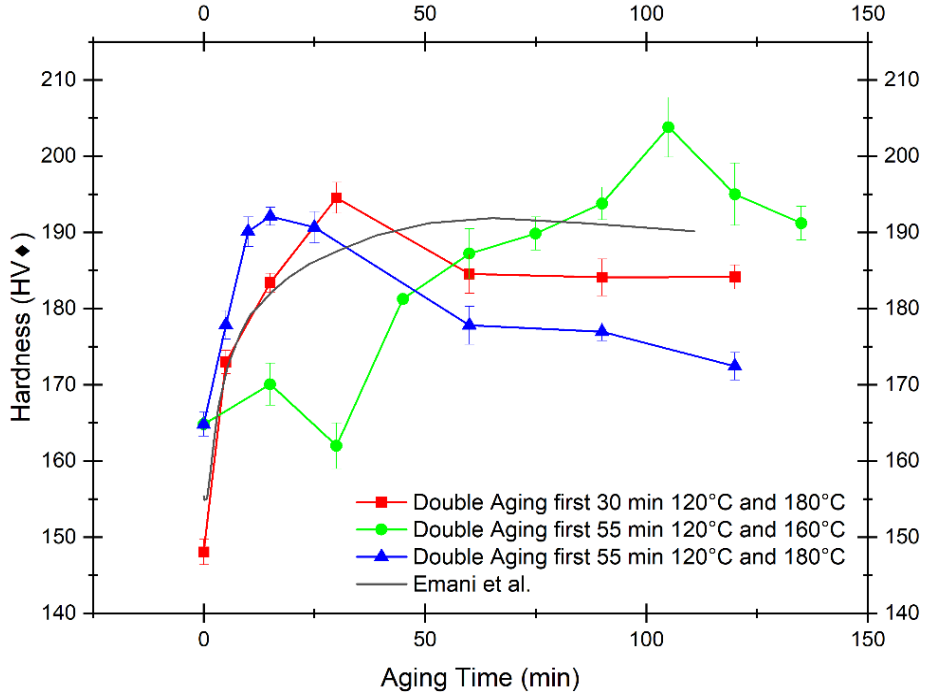

Figure 4.6: Microhardness over second step aging time for three different double aging treatments

4.3 Modeling the precipitation via TC-PRISMA

In this section, the results of multiple applications of the precipitation module (TC-PRISMA) for various parameters in the attempt of modeling the precipitation phenomena of one-step aging at 160°C, are presented and studied. Studying these results can lead to better understand the effects of the various parameters in precipitation hardening.

4.3.1 Simulation based on η' precipitates

4.3.1.1 Hardness evolution during precipitation

The results of the various applied compositions in hardness evolution during one-step aging at 160°C are presented in the following three figures 4.7-4.9. The supersaturation of the solid solution increases by increasing an alloying element's composition in the system. As a result, an increase in any of the four alloying elements' composition can increase the peak hardness by increasing the nucleation and growth rates, as the following figures show. However, the required time to reach the peak hardness remains the shame, according to the results. The amount that an addition of an alloying content can increase the peak hardness, differs from element to element. For example, zinc additions appear to enhance more efficiently the peak hardness than magnesium and copper. This enhancement, illustrated in Fig.4.7, is expressed by the increase in the peak hardness, reached in the same aging time.

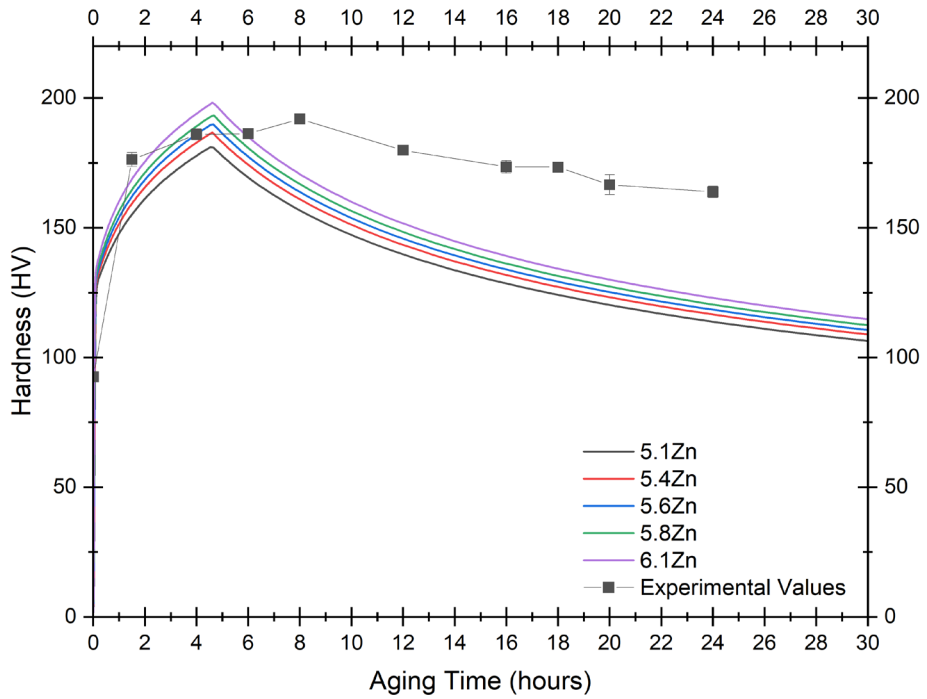

Figure 4.7: Hardness evolution over aging time for various zinc concentrations, 2.5%Mg and 1.6%Cu

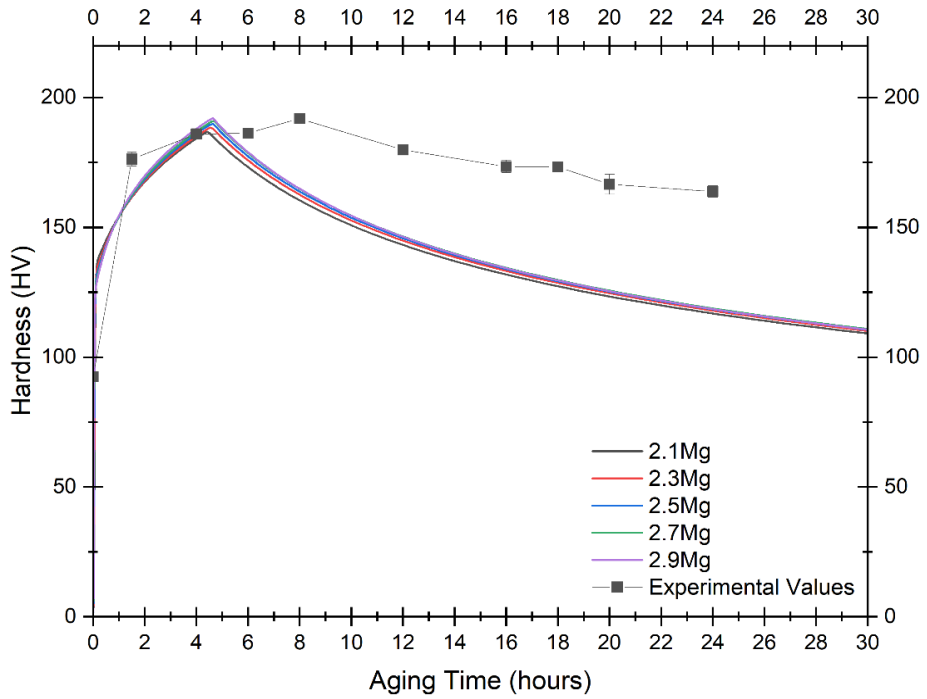

Figure 4.8: Hardness evolution over aging time for various magnesium concentrations, 5.6%Zn and 1.6%Cu

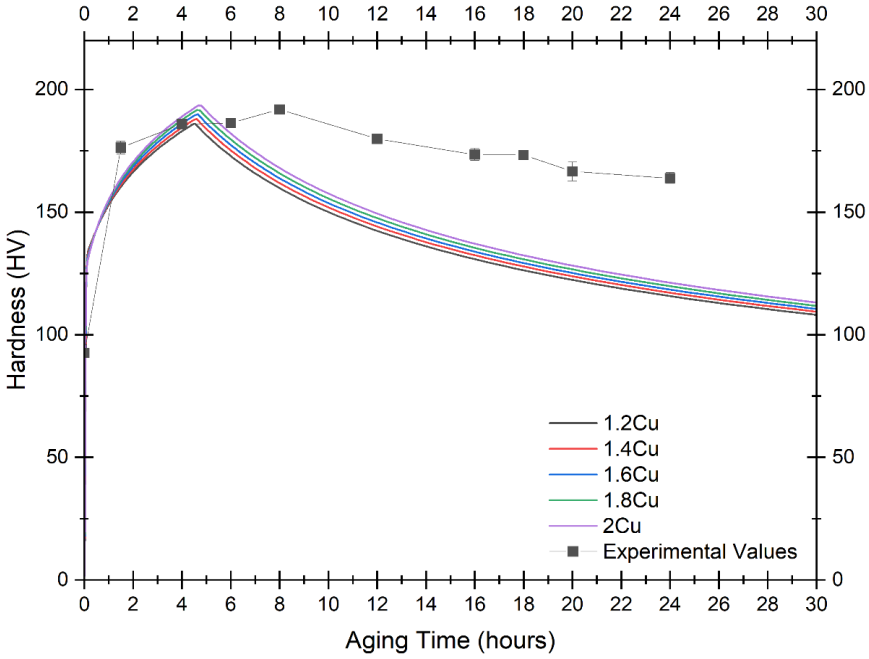

Figure 4.9: Hardness evolution over aging time for various copper concentrations, 5.6%Zn and 2.5%Mg

After many applications for various alloy compositions to approach the peak hardness, the Al-5.8Zn-2.3Mg- 1.6Cu alloy, presented in the Fig.4.10, was selected as the best approximation. The peak hardness value of this alloy is equal to 192HV, almost equal to the corresponding experimental value. A plate shape for η' precipitates with aspect ratio equal to 2.3 was applied to the selected alloy. This modification enhances the nucleation and growth rates, while the peak hardness remains the same, as the Fig.4.11 illustrates. The required time to reach the peak hardness, was approximated by modifications in the mobility enhancement prefactor. The best estimated time was equal to 7.6 hours and achieved with a prefactor equal to 0.25 after various attempts, the results of which are presented in the Fig.4.12.

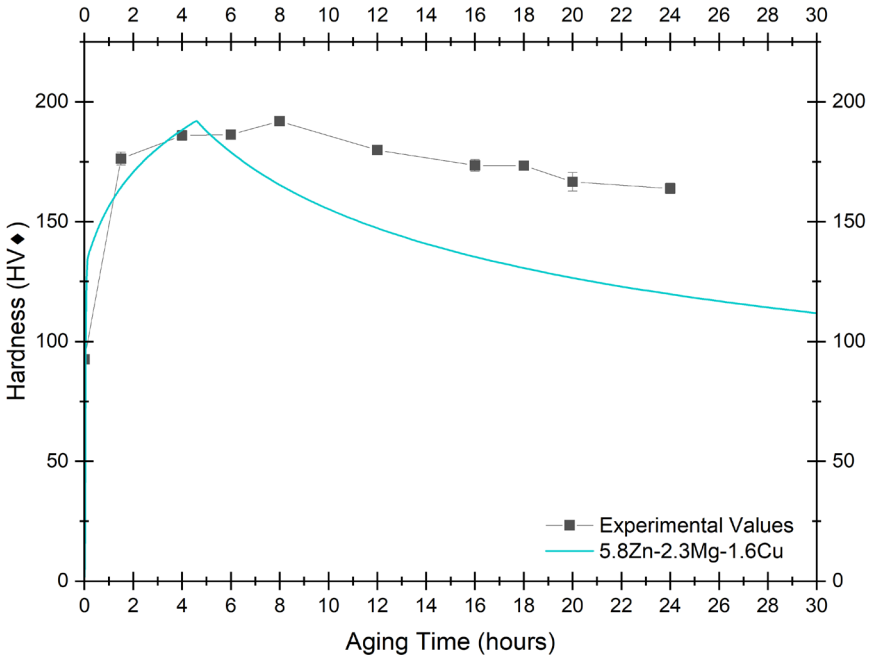

Figure 4.10: Hardness evolution over aging time for Al-5.8Zn-2.3Mg-1.6Cu alloy, in comparison with the corresponding experimental values.

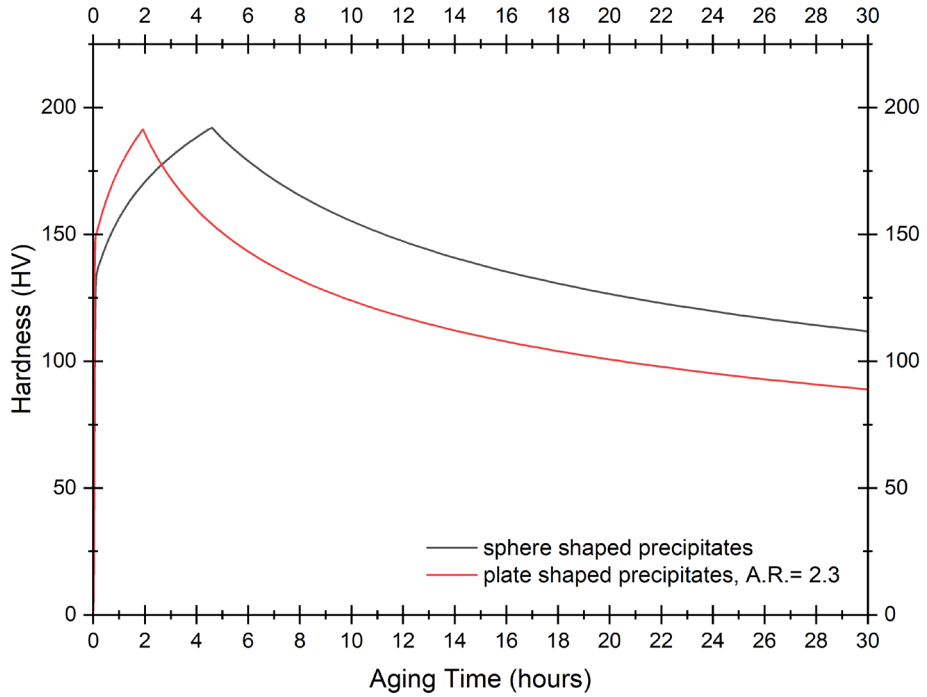

Figure 4.11: The effect of plate shaped η' precipitates with aspect ratio (A.R.) equal to 2.5 assumption in hardness evolution of the Al-5.8Zn-2.3Mg-1.6Cu alloy.

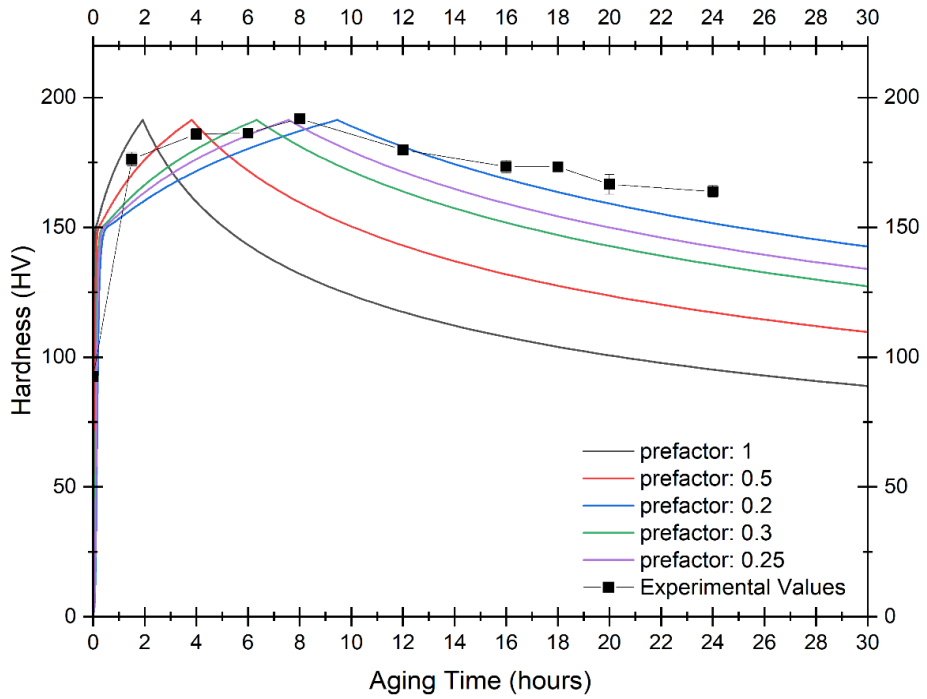

Figure 4.12: Hardness evolution over aging time for various mobility enhancement prefactors, Al-5.8Zn-2.3Mg-1.6Cu alloy.

4.3.1.2 Evolution of other characteristic quantities during aging

. The diagram in Fig.4.13, shows how an addition of the same amount of the three additional elements affect the nucleation rate of the η' precipitates. Even the nucleation rate is nullified in the second minute of aging for all compositions, a 0.2 mass percent addition of magnesium results in the highest nucleation rate in the start of precipitation. However, the higher the nucleation rate is in the start of the precipitation, the more rapidly reduces. Reducing the mobility prefactor leads to longer periods of nucleation but in lower nucleation rates in the initial stages, as can be observed in Fig.4.14.

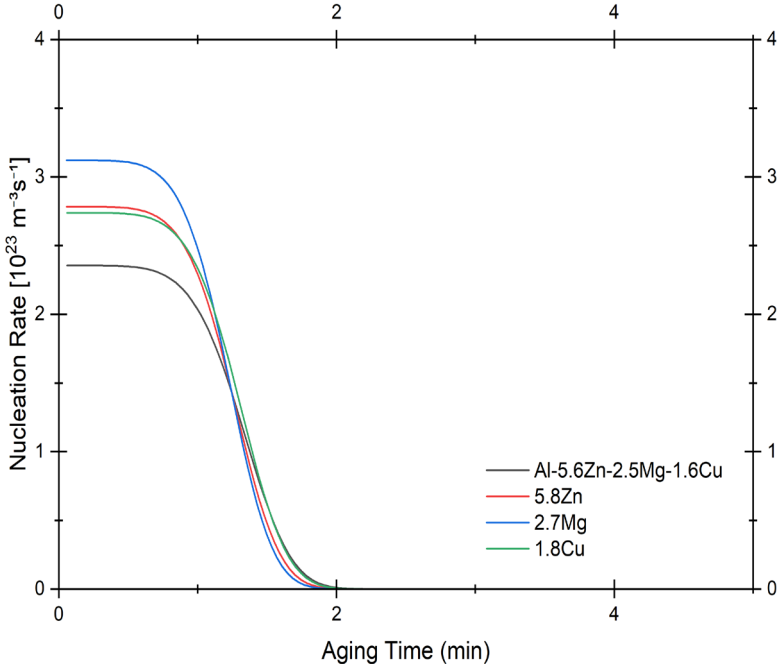

Figure 4.13: Effect of 0.2% w/w addition in zinc, magnesium and copper contents on the nucleation rate.

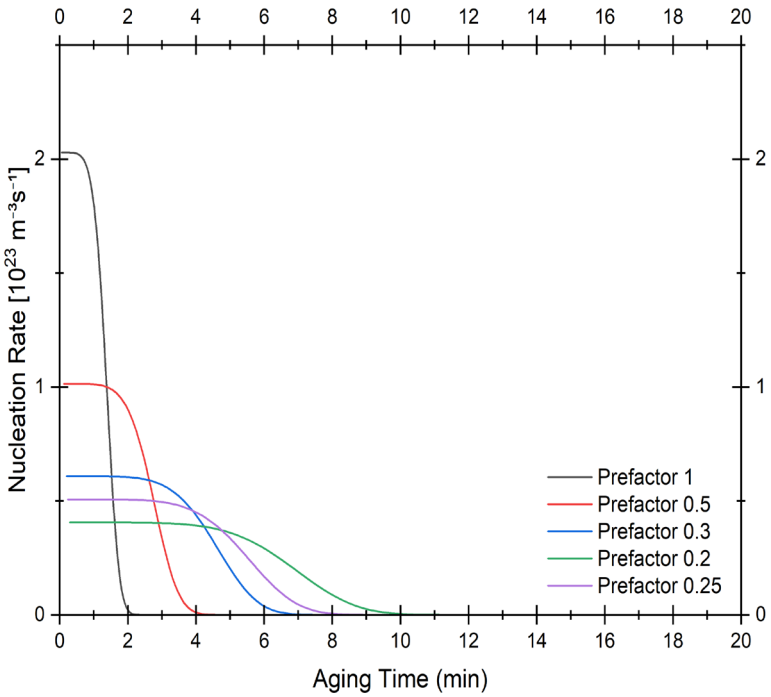

Figure 4.14: Effect of different mobility enhancement perfectors on the nucleation rate for the Al-5.8Zn-2.3Mg-1.6Cu alloy.

In the graph of Fig.4.15, the evolution of the nucleation rate, the number density of precipitates, and the normalized driving force for nucleation, as well as the way these quantities correlate during aging can be observed. In the start of precipitation, the nucleation rate and the driving force obtain the maximum values, as expected. By the end of nucleation, i.e., when the nucleation rate is nullified, the number density of precipitates, which expresses the number of particles per unit volume, is maximized. During growth, the number density is gradually reduced, probably because of the dissolution of some particles (e.g., subcritical nuclei). The driving force reduces rapidly during nucleation and in the initial stages of growth, because of the decrease in the supersaturation of the solid solution. Subsequently, the driving force continues to decrease but with an extremely low rate. Even the driving force for nucleation is never nullified during 30hrs aging, the nucleation stops when the driving force falls bellow the energy barrier for nucleation.

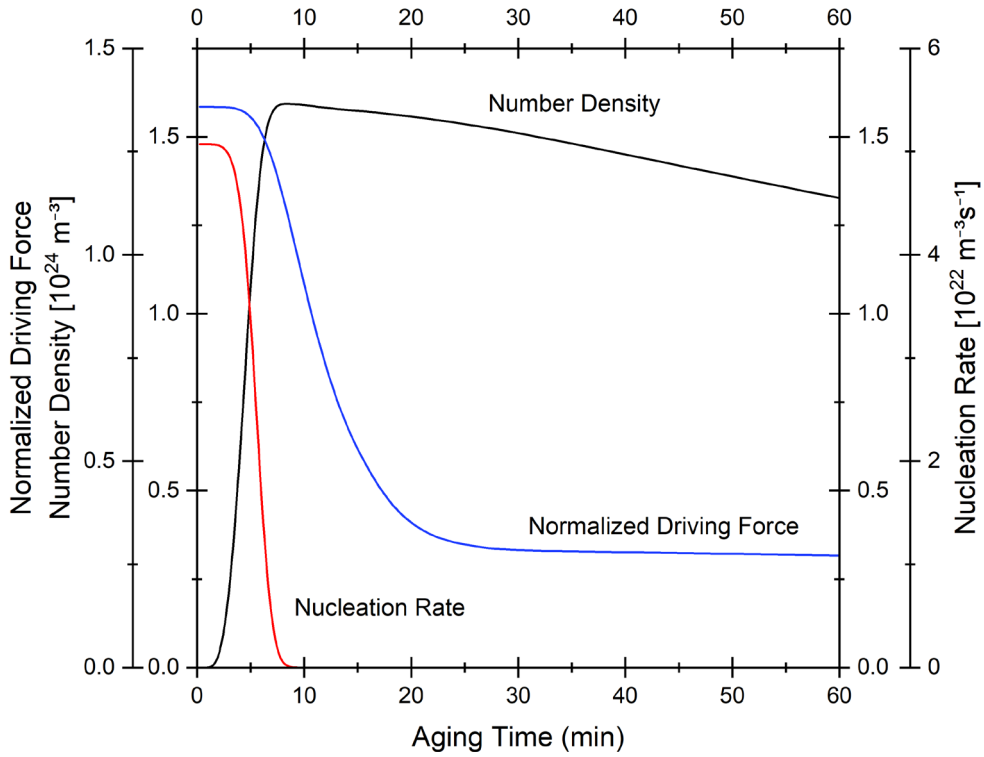

Figure 4.15: Evolution of number density, nucleation rate and normalized driving force during aging at 160°C for the Al-5.8Zn-2.3Mg-1.6Cu alloy.

The volume fraction of η' phase increases instantly in the start of nucleation reaching the value of 0.046 and continues to increase with a slow rate, as illustrated in Fig.4.16. Even the number density of the precipitates starts to reduce, the volume fraction continues to increase until the end of the treatment because of the particles' growth and coarsening. At peak hardness, the volume fraction is equal to 0.048 while the number density is 48×10^{13} particles per cubic nanometer.

In Fig.4.17, the size distributions of radius and length of the precipitates at peak hardness are presented. The majority of these plate-shaped precipitates (3×10^{32}) have 8.17nm length and 3.09nm radius, both into the range of limits reported in bibliography.

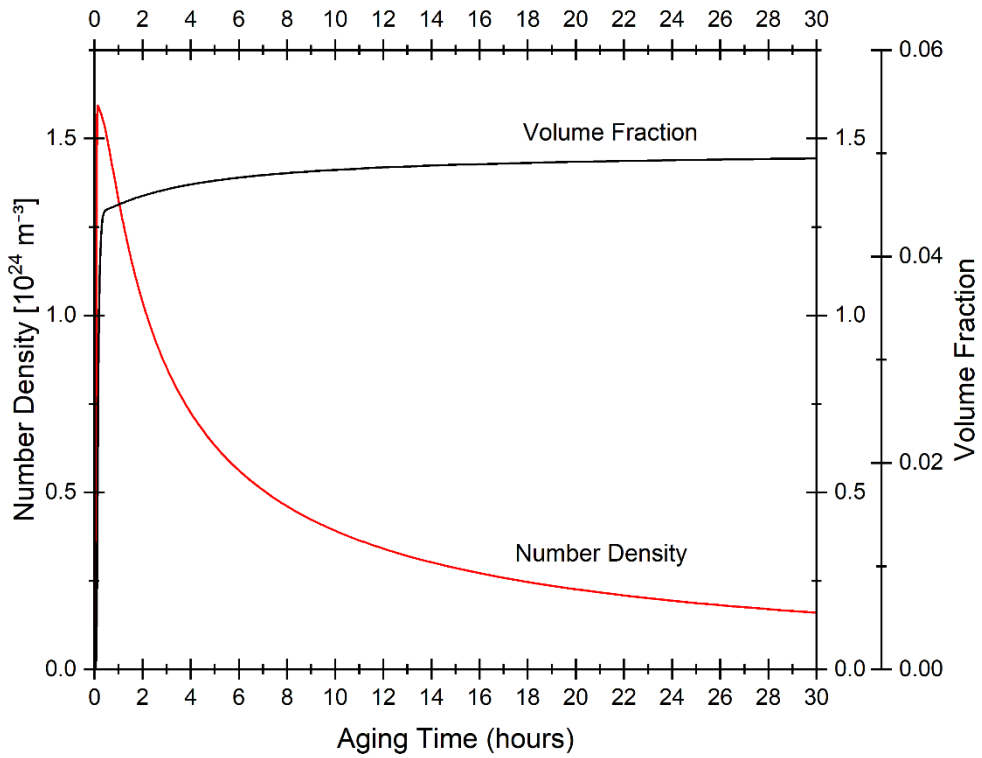

Figure 4.16: Evolution of number density and volume fraction during aging at 160°C for the Al-5.8Zn-2.3Mg-1.6Cu alloy.

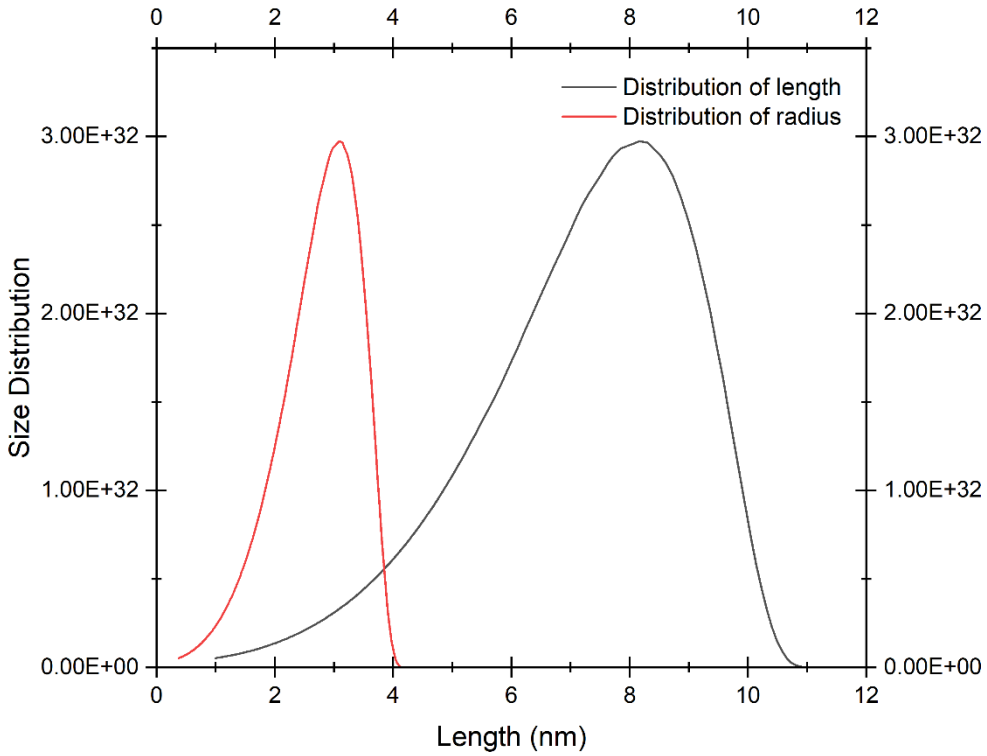

Figure 4.17: Size distributions of the radius and length of the precipitates for Al-5.8Zn-2.3Mg-1.6Cu alloy with plate-shaped precipitates (A.R.=2.3) and mobility prefactor 0.25.

The composition of the η' precipitates over aging time for Al-5.8Zn-2.3Mg-1.6Cu alloy is described by the Fig.4.18. The mass percent of aluminium and magnesium seem to remain almost steady at 12.8 and 14.86 respectively. However, the precipitates are gradually enriched in copper while getting poorer in zinc during nucleation and growth processes. At peak hardness, the composition in mass percent of the η' precipitates is (12.4)Al(64.1)Zn(14.9)Mg(8.6)Cu, according to the results.

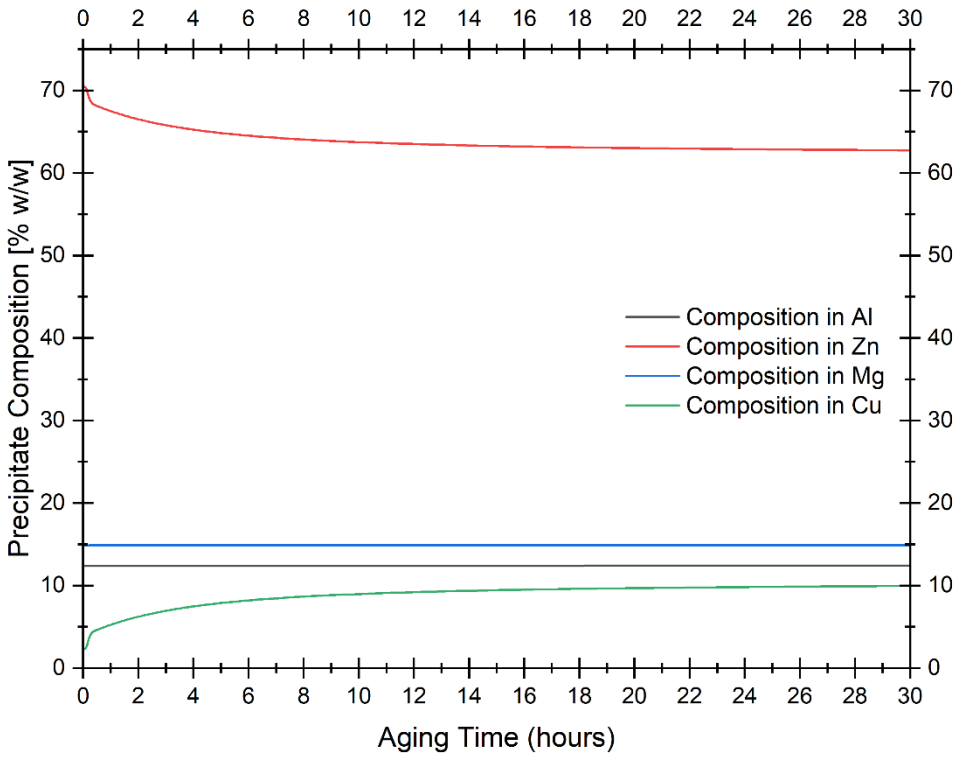

Figure 4.18: Precipitate Composition (% w/w) during aging, for Al-5.8Zn-2.3Mg-1.6Cu alloy with plate-shaped precipitates (A.R.=2.3) and mobility prefactor 0.25.

4.3.2 Simulation based on both η' and η precipitates

4.3.2.1 Hardness evolution during precipitation

Similar applications of the precipitation module for various alloy compositions and mobility enhancement prefactors, were proceeded to approach the one-step aging at 160°C of the 7075 aluminum alloy, with the assumption of two hardening phases, the metastable η' and the equilibrium η. The best approximation resulted for Al-5.8Zn-2.5Mg-1.2Cu alloy composition and a mobility prefactor equal to 1.35. The corresponded hardness curve is presented in Fig.4.19, the peak hardness is equal to 192.1HV, and reached in 7.8hrs.

The contributions of η' and η phase in total hardening of the material are illustrated in Fig.4.20. As the graph shows, the main hardening phase is metastable η' phase, giving a hardness of 190.7HV to the material after 7.8hrs aging. On the other hand, the equilibrium η phase contribution to hardening seems almost insignificant, since the highest hardness value that can give is equal to 3.57×10^{-6}HV after 30hrs aging. Note also that η phase hardening does no present a maximum during 30hrs of aging. These results come in accordance with the bibliography, where the η' and GP zones are considered the main hardening phases.

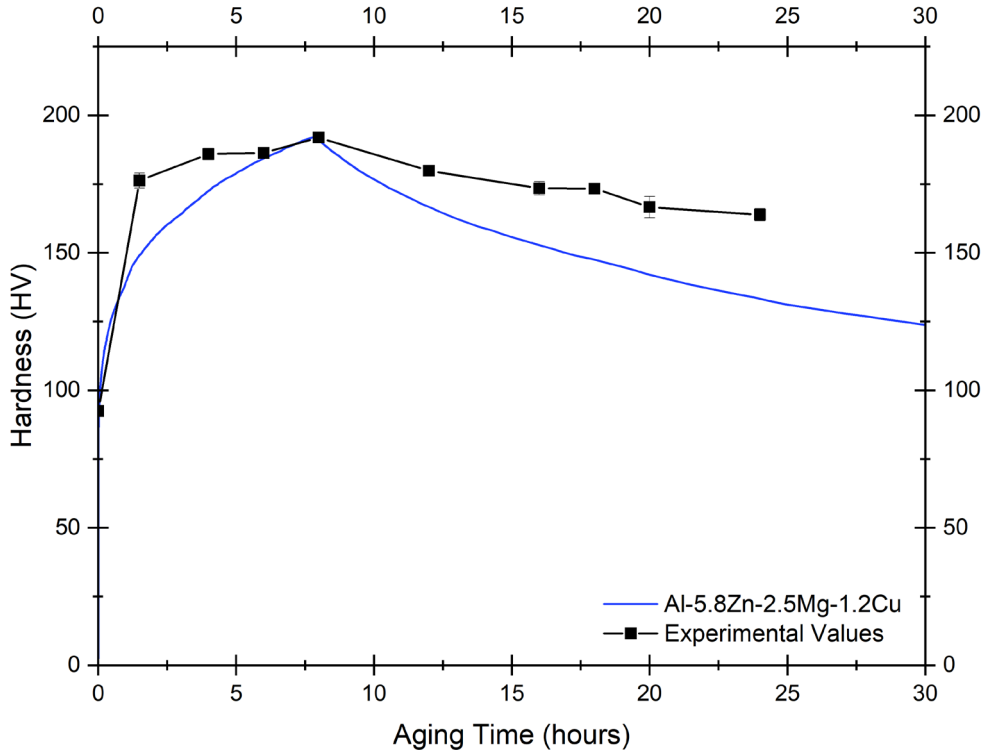

Figure 4.19: Hardness evolution over aging time for Al-5.8Zn-2.5Mg-1.2Cu alloy with mobility enhancement prefactor 1.35, in comparison with the corresponding experimental values.

Figure 4.20: Hardening contribution of the η' and η phase over aging time for Al-5.8Zn-2.5Mg-1.2Cu alloy.

4.3.2.2 Evolution of other characteristic quantities during aging

The nucleation process for both η' and η phases happen extremely fast in this approach, as the Fig.4.21 presents. For the metastable η' phase, the nucleation almost ends in 24sec, while the nucleation of the equilibrium phase η in 18sec. The nucleation rate of η' is extremely higher than this of η phase, the former is in the order of 10^{26} $m^{-3}s^{-1}$, while the latter in the order of 10^{13} $m^{-3}s^{-1}$. This huge deviation occurs due to the much higher interfacial energy of the incoherent η phase (0.2 J/mol) than this of the semicoherent η phase (0.06 J/mol).

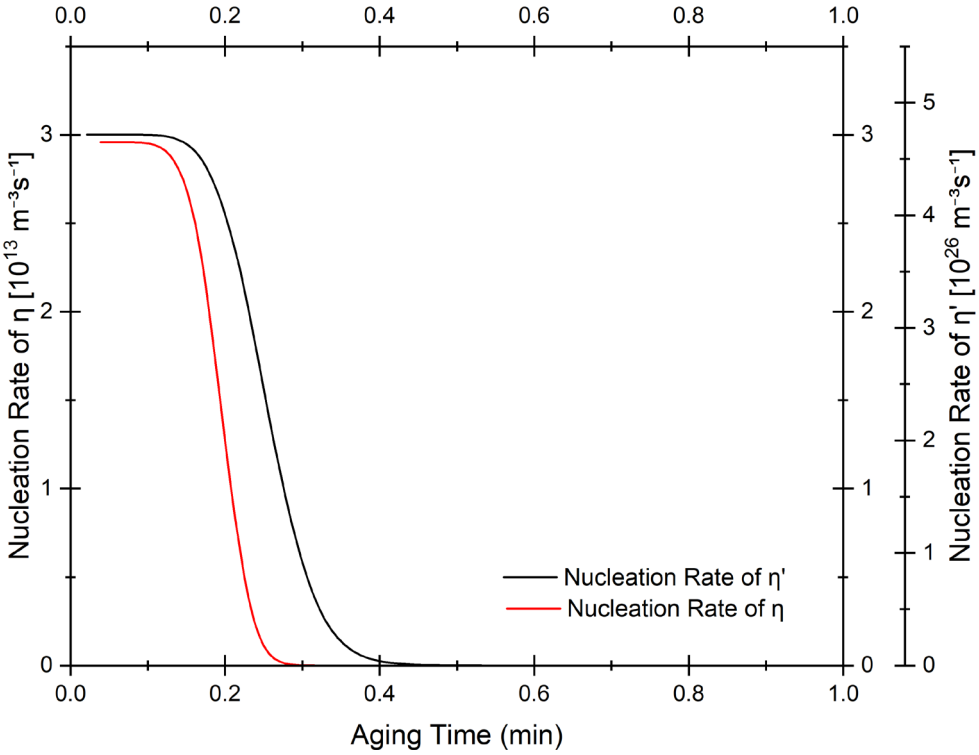

Figure 4.21: Nucleation rates of the η' and η phase over aging time for Al-5.8Zn-2.5Mg-1.2Cu alloy.

In Fig.4.22 and Fig.4.23, for η' and η respectively, the evolution of the nucleation rate, the number density of precipitates, and the normalized driving force for nucleation, as well as their correlation are presented. The driving force for precipitation is instantly reduced in the very first seconds of aging. By the end of η' nucleation, the number density of precipitates has reached its maximum value 38.8×10^{15} nm^{-3}, much more than it was in the first approach. On the other hand, the number density in this approach, seems to decrease more rapidly than the first approach. The correlation of these three quantities is similar for both phases, although the even rapid decrease in the driving force for nucleation of η phase stops at a higher driving force value. This indicates the higher nucleation energy barrier of η phase because of its high interfacial energy. In addition, the maximum number density of η precipitates is extremely lower than the corresponding value of η' phase, equal to 13.1 nm^{-3}, indicating the insignificant contribution in hardening of η phase. Another observation for the number density of η phase is that decreases extremely fast and is nearly nullified after the first two minutes of aging.

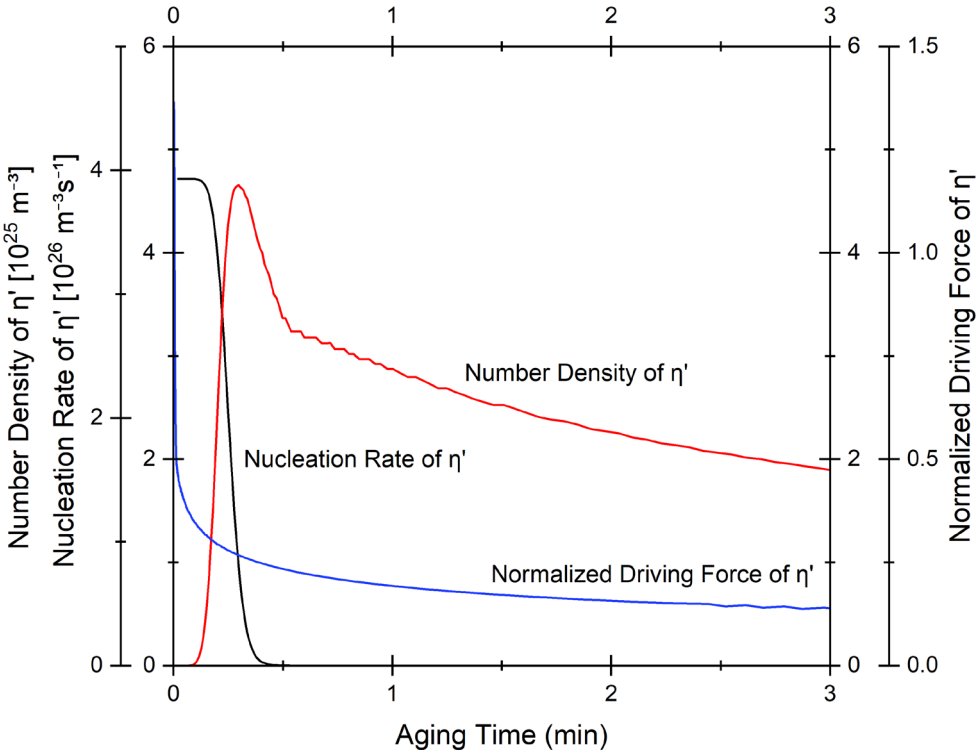

Figure 4.22: Evolution of number density, nucleation rate and normalized driving force of η' phase during aging at 160°C for the Al-5.8Zn-2.5Mg-1.2Cu alloy.

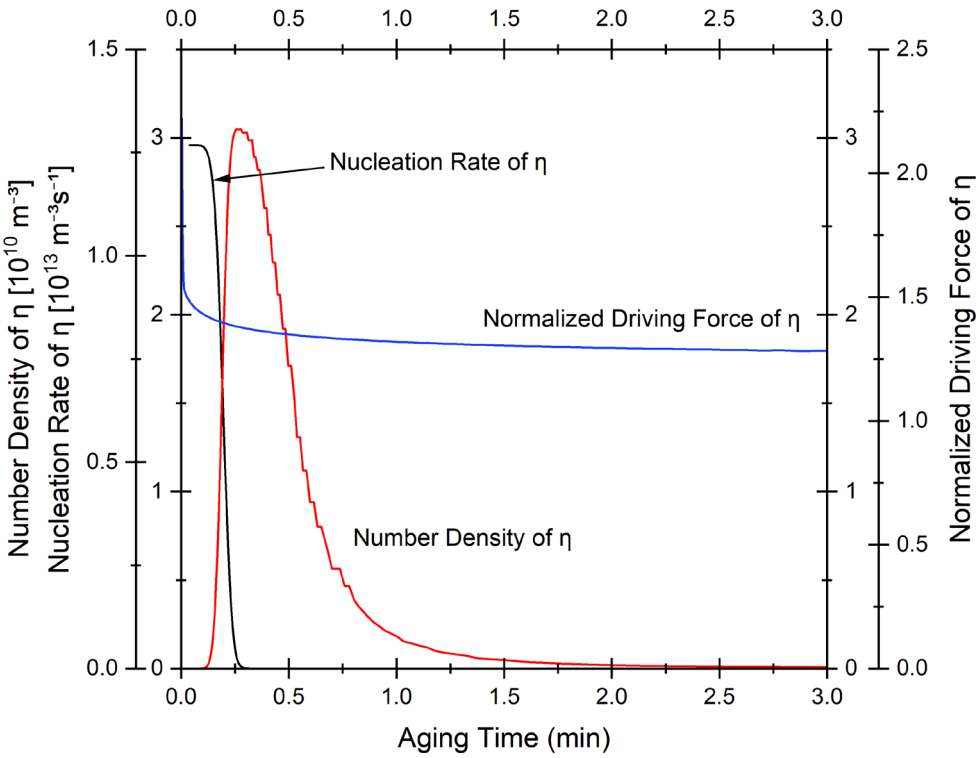

Figure 4.23: Evolution of number density, nucleation rate and normalized driving force of η phase during aging at 160°C for the Al-5.8Zn-2.5Mg-1.2Cu alloy.

In the Fig.4.24 the volume fraction evolution for the two phases, is illustrated. Because of the extremely rapid nucleation of η' in the start of precipitation, its volume fraction reaches almost instantly the value 0.043 and remains almost steady afterwards. The volume fraction of the η phase is insignificantly small during the precipitation, however it seems that for larger aging time it would continue to slowly increase, since no maximum presents during 30hrs of aging.

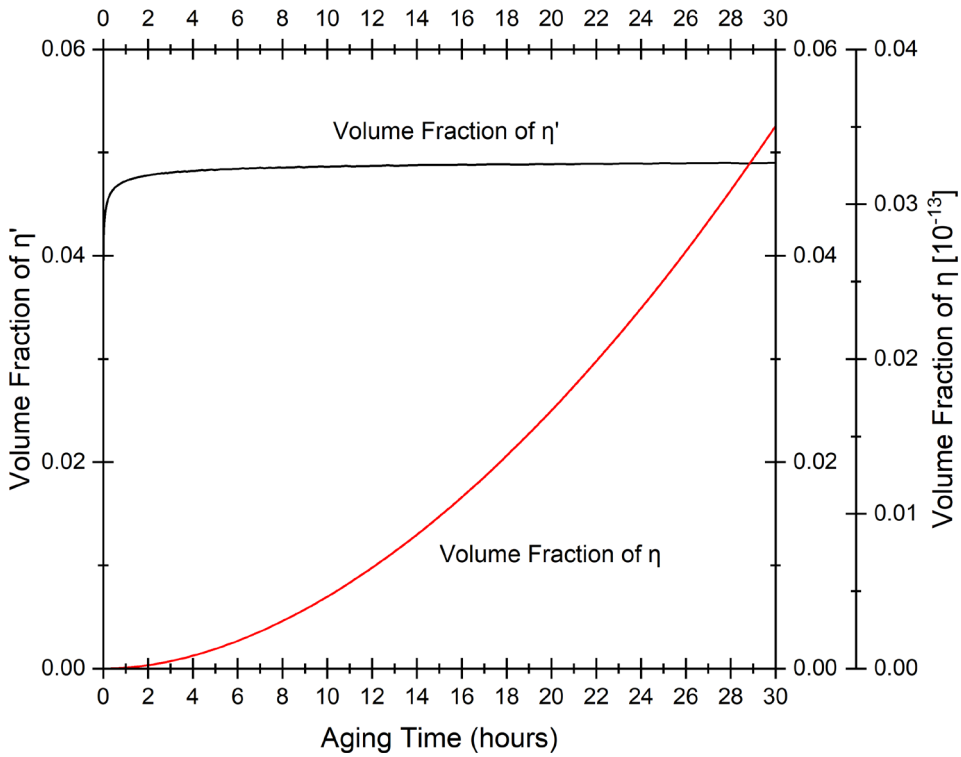

Figure 4.24: Evolution of volume fractions of η' and η phase during aging at 160°C for the Al-5.8Zn-2.5Mg-1.2Cu alloy.

The size distribution of the radius of precipitates for the two phases is presented in the Fig.4.25. At peak hardness, a high number of η' precipitates exist according to the graph with radius in the range of 0.5 to 5.2nm. As expected by the previous results, the number of precipitates at peak hardness is extremely small, and their radius takes values of a shorter range (3.9 to 4.8nm). The majority of η precipitates obtain a radius of 3.5nm, while the majority of the larger in size η precipitates obtain a radius of 4.5nm.

The compositions of the η' and η precipitates during aging time differs significantly, as can observed in the following two figures (Fig.4.25 and Fig.4.26). In the η phase composition, magnesium is the content with the smallest mass percent (14.9% at peak hardness), while the enrichment in copper against zinc is much more intense than it is in the η' phase. At peak hardness the chemical composition of η' phase is (12.4)Al(64.38)Zn(14.89)Mg(8.33)Cu, while that of η phase is (21.7)Al(23.68)Zn(20.67)Mg(33.94)Cu.

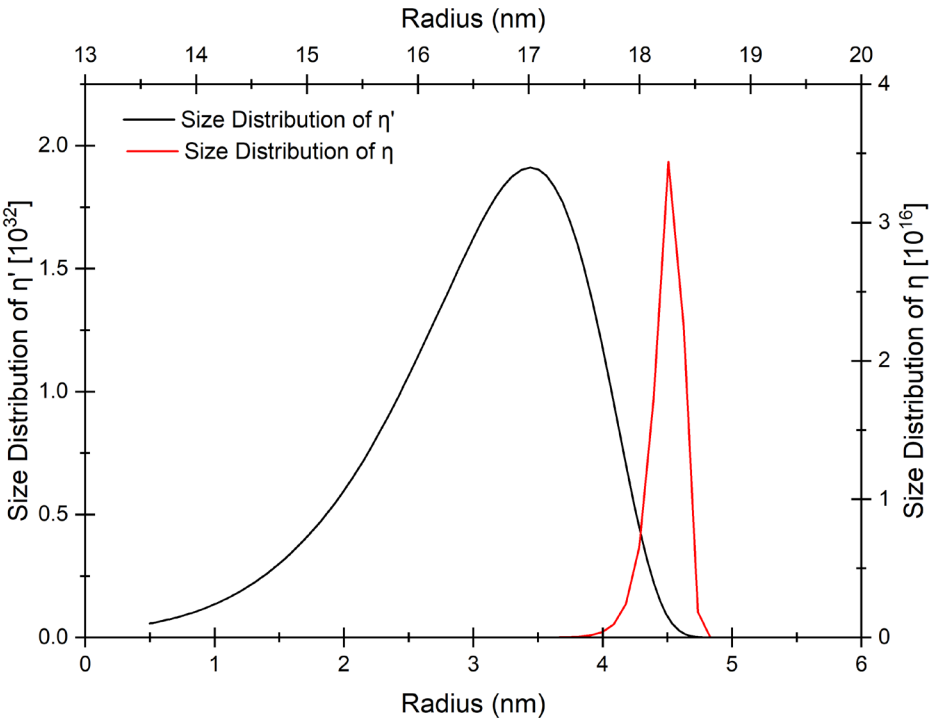

Figure 4.25: Radius size distribution of η' and η phase at peak hardness of the Al-5.8Zn-2.5Mg-1.2Cu alloy.

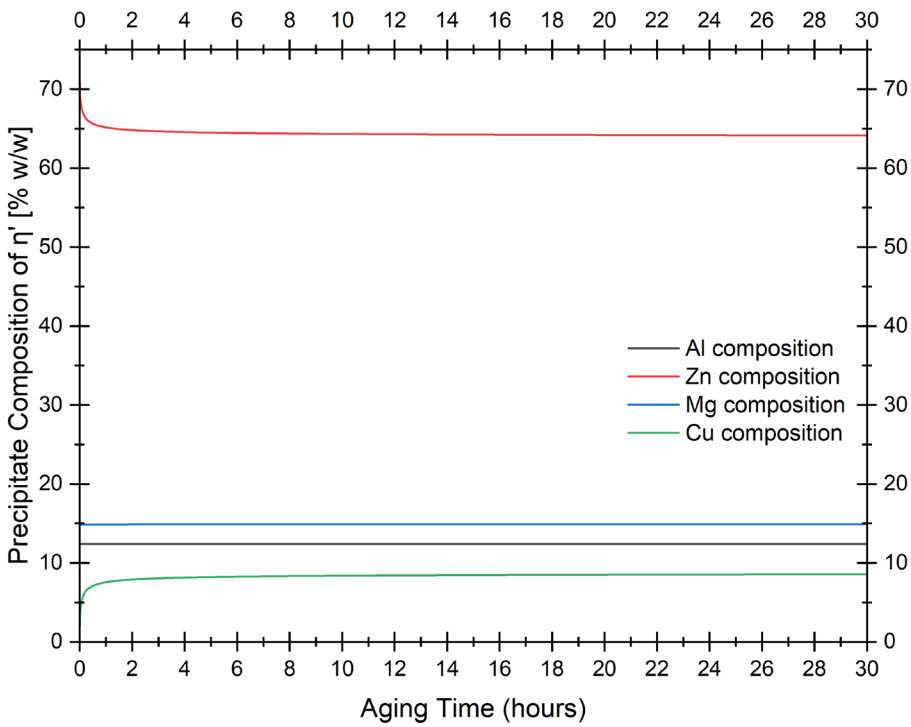

Figure 4.26: η' precipitate composition (% w/w) during aging, for Al-5.8Zn-2.5Mg-1.2Cu alloy.

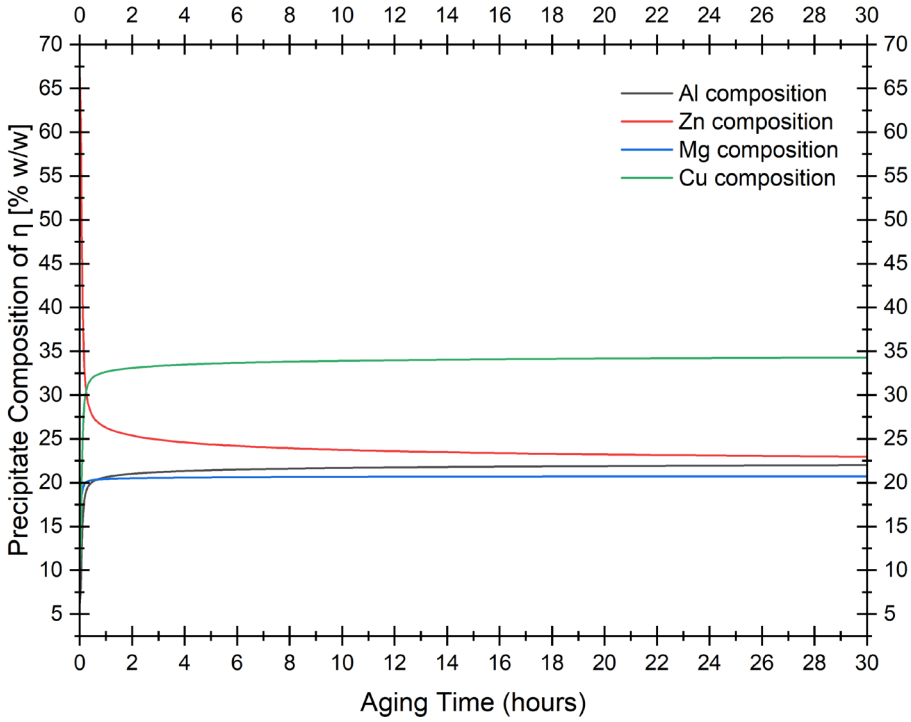

Figure 4.27: η precipitate composition (% w/w) during aging, for Al-5.8Zn-2.5Mg-1.2Cu alloy.

Chapter 5 Conclusions

The microstructure of the aluminum alloy 7075, during aging precipitation was studies via optical metallography, microhardness measurements and modeling with the TC-PRISMA precipitation model. The results of this study may be found helpful to aging treatments designing and applications, as well as to subsequent research on heat treatable aluminum alloys behavior in precipitation.

The results of the microhardness measurements for three different aging heat treatments showed that the alloy AA7075 had good response in the one-step aging at 160°C, reaching at peak hardness the value of 191.9HV in a reasonable time of 8hrs. However, duplex-aging treatments had even better results for both peak hardness and aging time. The highest peak hardness was obtained in the treatment of 55min pre-aging at 120°C, and aging at 160°C. The peak hardness value was 203.8HV, and it was reached in 160min total aging time (55min+105min). In this treatment, two peaks of hardness were observed, indicating the partial reversion phenomenon, reported many times in bibliography for 7xxx series alloys.

In both approaches of the one-step aging treatment via the TC-PRISMA precipitation module, a good accordance with the experimental results was achieved. The peak hardness was approached with almost absolute accuracy, while relative low deviations were observed in the rates of gaining and losing hardness. In the first approach, where the metastable η' phase was assumed as the only hardening phase, the results for various characteristic quantities showed that at peak hardness the volume fraction of η phase is equal to 0.048 and the majority of precipitates had radius equal to 3.09nm and length equal to 8.17nm. The chemical composition of η' precipitates was found Al(64.38)Zn(14.89)Mg(8.33)Cu in mass percent. In the approach with the assumption of the two hardening phases η' and equilibrium η, the contribution of η phase to hardening was found insignificant. This agrees with the fact that η' and maybe GP zones are the main hardening phases in the precipitation aging of 7xxx alloy series. As incoherent phase, the equilibrium η phase obtains high interfacial energy and requires first the formation of coherent and semicoherent precipitates. This can explain the fact that its volume fraction had not reach a maximum during 30hrs of aging. At peak hardness of the second approach only a little number of η precipitates were presented with large radius sizes in the range of 13.6 to 18.7nm, while η precipitates dominated with radius sizes in the range of 0.5 to 5.2nm. The chemical compositions were calculated as Al(64.38)Zn(14.89)Mg(8.33)Cu and Al(23.68)Zn(20.67)Mg(33.94)Cu for η' and η, respectively.

Further investigation is required for more accurate values of precipitation module parameters. For instance, this investigation could include:

- Metallography with electronic microscopes (SEM, TEM, HREM) for observation and identification of the tiny particles (hardening precipitates, or dispersoids), and their characteristic quantities (structure, size, chemical composition and morphology)
- Differential Scanning Calorimetry (DSC) technique to characterize the reactions that occur during dissolution or formation of precipitates, by interpreting thermograms for various aging states of the material.

In addition, different and more complex aging treatments can apply to the AA7075 alloy in order to examine further its response to heat treatments. A suggesting treatment could be a thermomechanical double aging, during which mechanical strain is introduced to the alloy, after the solution and quenching treatments or between the first and second aging step. Such treatments have been proved to lead to strength values close to the T6 temper, as well as to better results in fatigue and stress

corrosion resistance [17]. Attempts to simulate these complex treatments in subsequent investigations, would also be of high scientific importance.

Chapter 6 References

[1] N.Q. Chinh, J. Lendvai, D.H. Ping, K. Hono, The effect of Cu on mechanical and precipitation properties of Al–Zn–Mg alloys, J. Alloys Compd. 378 (2004) 52–60. https://doi.org/10.1016/j.jallcom.2003.11.175.

[2] E.L. Rooy, Introduction to Aluminum and Aluminum Alloys, in: ASM Handbook Committee (Ed.), Prop. Sel. Nonferrous Alloys Spec.-Purp. Mater., ASM International, 1990: p. 0. https://doi.org/10.31399/asm.hb.v02.a0001057.

[3] A. Deschamps, Y. Bréchet, F. Livet, Influence of copper addition on precipitation kinetics and hardening in Al-Zn-Mg alloy, (1999).

[4] Γ.Ν. ΧΑΪΔΕΜΕΝΟΠΟΥΛΟΣ, ΦΥΣΙΚΗ ΜΕΤΑΛΛΟΥΡΓΙΑ, ΕΚΔΟΣΕΙΣ ΤΖΙΟΛΑ, n.d.

[5] G.H. Koch, D.T. Kolijn, The Heat Treatment of the Commercisl Aluminum Alloy 7075, (1979).

[6] G.E. Totten, ed., Principles of Heat Treating of Nonferrous Alloys, in: Heat Treat. Nonferrous Alloys, ASM International, 2016: pp. 3–31. https://doi.org/10.31399/asm.hb.v04e.a0006250.

[7] A. Deschamps, Y. Bréchet, Influence of quench and heating rates on the ageing response of an Al–Zn–Mg–(Zr) alloy, Mater. Sci. Eng. A. 251 (1998) 200–207. https://doi.org/10.1016/S0921-5093(98)00615-7.

[8] R.N. Lumley, A.J. Morton, R.G. O'Donnell, I.J. Polmear, NEW HEAT TREATMENTS FOR AGE-HARDENABLE ALUMINUM ALLOYS, (2005) 7.

[9] M. Chemingui, M. Khitouni, K. Jozwiak, G. Mesmacque, A. Kolsi, Characterization of the mechanical properties changes in an Al–Zn–Mg alloy after a two-step ageing treatment at 70° and 135°C, Mater. Des. 31 (2010) 3134–3139. https://doi.org/10.1016/j.matdes.2009.12.033.

[10] D.A. Porter, K.E. Easterling, M.Y. Sherif, Phase transformations in metals and alloys, 3rd ed, CRC Press, Boca Raton, FL, 2009.

[11] J. Lendvai, The Effect of Vacancy-rich Clusters on the Decomposition Processes in Al-Zn-Mg Alloys, (1984).

[12] H. Loffler, Review Decomposition processes in AI-Zn-Mg alloys, (1983) 26.

[13] J.D. Embury, R.B. Nicholson, The nucleation of precipitates: The system Al-Zn-Mg, Acta Metall. 13 (1965) 403–417. https://doi.org/10.1016/0001-6160(65)90067-2.

[14] T. Ogura, S. Hirosawa, A. Cerezo, T. Sato, Atom probe tomography of nanoscale microstructures within precipitate free zones in Al–Zn–Mg(–Ag) alloys, Acta Mater. 58 (2010) 5714–5723. https://doi.org/10.1016/j.actamat.2010.06.046.

[15] J.Z. Liu, J.H. Chen, X.B. Yang, S. Ren, C.L. Wu, H.Y. Xu, J. Zou, Revisiting the precipitation sequence in Al–Zn–Mg-based alloys by high-resolution transmission electron microscopy, Scr. Mater. 63 (2010) 1061–1064. https://doi.org/10.1016/j.scriptamat.2010.08.001.

[16] Y.H. Zhao, X.Z. Liao, Z. Jin, R.Z. Valiev, Y.T. Zhu, Microstructures and mechanical properties of ultrafine grained 7075 Al alloy processed by ECAP and their evolutions during annealing, Acta Mater. 52 (2004) 4589–4599. https://doi.org/10.1016/j.actamat.2004.06.017.

[17] S.V. Emani, J. Benedyk, P. Nash, D. Chen, Double aging and thermomechanical heat treatment of AA7075 aluminum alloy extrusions, J. Mater. Sci. 44 (2009) 6384–6391. https://doi.org/10.1007/s10853-009-3879-8.

[18] L.K. Berg, J. Gjønnes, V. Hansen, X.Z. Li, M. Knutson-Wedel, G. Waterloo, D. Schryvers, L.R. Wallenberg, GP-zones in Al–Zn–Mg alloys and their role in artificial aging, Acta Mater. 49 (2001) 3443–3451. https://doi.org/10.1016/S1359-6454(01)00251-8.

[19] R. Ferragut, A. Somoza, A. Tolley, Microstructural evolution of 7012 alloy during the early stages of artificial ageing, Acta Mater. 47 (1999) 4355–4364. https://doi.org/10.1016/S1359-6454(99)00315-8.

[20] Y. Zou, X. Wu, S. Tang, Q. Zhu, H. Song, L. Cao, Co-precipitation of T' and η' phase in Al-Zn-Mg-Cu alloys, (2020).

[21] N. Afify, A.-F. Gaber, G. Abbady, Fine Scale Precipitates in Al-Mg-Zn Alloys after Various Aging Temperatures, Mater. Sci. Appl. 02 (2011) 427–434. https://doi.org/10.4236/msa.2011.25056.

[22] A. Bigot, P. Auger, S. Chambreland, D. Blavette, A. Reeves, Atomic Scale Imaging and Analysis of T' Precipitates in Al-Mg-Zn Alloys, Microsc. Microanal. Microstruct. 8 (1997) 103–113. https://doi.org/10.1051/mmm:1997109.
[23] A. Kverneland, V. Hansen, G. Thorkildsen, H.B. Larsen, P. Pattison, X.Z. Li, J. Gjønnes, Transformations and structures in the Al–Zn–Mg alloy system: A diffraction study using synchrotron radiation and electron precession, Mater. Sci. Eng. A. 528 (2011) 880–887. https://doi.org/10.1016/j.msea.2010.10.001.
[24] X. Fang, Y. Du, M. Song, K. Li, C. Jiang, Effects of Cu content on the precipitation process of Al–Zn–Mg alloys, J. Mater. Sci. 47 (2012) 8174–8187. https://doi.org/10.1007/s10853-012-6714-6.
[25] O.B.M. Hardouin Duparc, The Preston of the Guinier-Preston Zones. Guinier, Metall. Mater. Trans. B. 41 (2010) 925–934. https://doi.org/10.1007/s11663-010-9387-z.
[26] A.K. Mukhopadhyay, Guinier-Preston zones in a high-purity Al-Zn-Mg alloy, Philos. Mag. Lett. 70 (1994) 135–140. https://doi.org/10.1080/09500839408240966.
[27] K. Hono, N. Sano, T. Sakurai, Quantitative atom-probe analysis of some aluminum alloys, (1991) 8.
[28] S.K. Maloney, K. Hono, I.J. Polmear, S.P. Ringer, The chemistry of precipitates in an aged Al-2.1Zn-1.7Mg at.% alloy, Scr. Mater. 41 (1999) 1031–1038. https://doi.org/10.1016/S1359-6462(99)00253-5.
[29] G. Jürgens, M. Kempe, H. Löffler, On the kinetics of the growth of Guinier–Preston zones in Al□Zn□Mg alloys, Phys. Status Solidi A. 25 (1974) K73–K76. https://doi.org/10.1002/pssa.2210250154.
[30] G. Groma, E. Kovács-cseténYi, I. Kovács, J. Lendvai, T. Ungár, The composition of Guinier–Preston zones in Al–Zn–Mg alloys, Philos. Mag. A. 40 (1979) 653–665. https://doi.org/10.1080/01418617908234866.
[31] G. Dlubek, O. Brummer, R. Krause, A. Baranowski, B. Rozenfeld, A positron study of Guinier-Preston zones and precipitates in Al-Zn alloys having Mg or Ge additions, (1983).
[32] G. Dlubek, R. Krause, O. Brummer, Study of formation and reversion of Guinier-Preston zones in Al-1.5 at % Zn-x at % Mg alloys by positrons, (1986).
[33] X.J. Jiang, J. Tafto, B. Noble, B. Holme, G. Waterloo, Differential scanning calorimetry and electron diffraction investigation on low-temperature aging in Al-Zn-Mg alloys, Metall. Mater. Trans. A. 31 (2000) 339–348. https://doi.org/10.1007/s11661-000-0269-x.
[34] C. Wolverton, Crystal structure and stability of complex precipitate phases in Al–Cu–Mg–(Si) and Al–Zn–Mg alloys, Acta Mater. 49 (2001) 3129–3142. https://doi.org/10.1016/S1359-6454(01)00229-4.
[35] X.Z. Li, V. Hansen, J. Gjønnes, L.R. Wallenberg, HREM study and structure modeling of the η' phase, the hardening precipitates in commercial Al-Zn-Mg alloys, (1999).
[36] J. Simensens, J. Gjønnes, AN ELECTRON MICROSCOPE INVESTIGATION OF THE MICROSTRUCTURE IN AN ALUMINIUM-ZINC-MAGNESIUM ALLOY, ACTA Metall. 18 (1970) 10.
[37] D. Godard, P. Archambault, E. Aeby-Gautier, G. Lapasset, Precipitation sequences during quenching of the AA 7010 alloy, Acta Mater. 50 (2002) 2319–2329. https://doi.org/10.1016/S1359-6454(02)00063-0.
[38] H.C. Fang, H. Chao, K.H. Chen, Effect of Zr, Er and Cr additions on microstructures and properties of Al–Zn–Mg–Cu alloys, Mater. Sci. Eng. A. 610 (2014) 10–16. https://doi.org/10.1016/j.msea.2014.05.021.
[39] L. Ding, L. Zhao, Y. Weng, D. Schryvers, Q. Liu, H. Idrissi, Atomic-scale investigation of the heterogeneous precipitation in the E (Al18Mg3Cr2) dispersoid of 7075 aluminum alloy, J. Alloys Compd. 851 (2021) 156890. https://doi.org/10.1016/j.jallcom.2020.156890.
[40] J. Herrnring, B. Sundman, P. Staron, B. Klusemann, Modeling precipitation kinetics for multi-phase and multi-component systems using particle size distributions via a moving grid technique, Acta Mater. 215 (2021) 117053. https://doi.org/10.1016/j.actamat.2021.117053.
[41] Precipitation Module (TC-PRISMA) User Guide, (n.d.) 182.

[42] ASM handbook. 9: Metallography and microstructures, 1. print, ASM International, Materials Park, Ohio, 2004.
[43] W. Yang, S. Ji, M. Wang, Z. Li, Precipitation behaviour of Al-Zn-Mg-Cu alloy and diffraction analysis from η' precipitates in four variants, (2014).
[44] Origin: Data Analysis and Graphing Software, (n.d.). https://www.originlab.com/index.aspx?go=Products/Origin (accessed September 15, 2022).
[45] N. Kamp, A. Sullivan, R. Tomasi, J.D. Robson, Modelling Heterogeneous Precipitation in 7xxx Aluminium Alloys during Complex Processing, Mater. Sci. Forum. 519–521 (2006) 1435–1440. https://doi.org/10.4028/www.scientific.net/MSF.519-521.1435.
[46] S. Kalpakjian, S.R. Schmid, ΜΗΧΑΝΟΥΡΓΙΚΗ Επιστήμη και Τεχνολογία, 7th ed., ΤΖΙΟΛΑΣ, n.d.